

GIScience & Remote Sensing

ISSN: 1548-1603 (Print) 1943-7226 (Online) Journal homepage: www.tandfonline.com/journals/tgrs20

Mapping desert shrubs in Inner Mongolia using universal medium resolution satellite imagery: development of new spectral indices

Zhijun Fu, Bingfang Wu, Hongwei Zeng & Mengxiao Li

To cite this article: Zhijun Fu, Bingfang Wu, Hongwei Zeng & Mengxiao Li (2025) Mapping desert shrubs in Inner Mongolia using universal medium resolution satellite imagery: development of new spectral indices, GIScience & Remote Sensing, 62:1, 2428366, DOI: 10.1080/15481603.2024.2428366

To link to this article: https://doi.org/10.1080/15481603.2024.2428366

© 2024 The Author(s). Published by Informa UK Limited, trading as Taylor & Francis Group.

View supplementary material

Published online: 13 Dec 2024.

Submit your article to this journal

Article views: 3425

View related articles

View Crossmark data

Citing articles: 8 View citing articles

Full Terms & Conditions of access and use can be found at
https://www.tandfonline.com/action/journalInformation?journalCode=tgrs20

GISCIENCE & REMOTE SENSING
2025, VOL. 62, NO. 1, 2428366
https://doi.org/10.1080/15481603.2024.2428366

Taylor & Francis
Taylor & Francis Group

OPEN ACCESS Check for updates

Mapping desert shrubs in Inner Mongolia using universal medium resolution satellite imagery: development of new spectral indices

Zhijun Fu[a,b], Bingfang Wu[a,b], Hongwei Zeng[a,b] and Mengxiao Li[a]

[a]State Key Laboratory of Remote Sensing Science, Aerospace Information Research Institute, Chinese Academy of Sciences, Beijing, China; [b]College of Resources and Environment, University of Chinese Academy of Sciences, Beijing, China

ABSTRACT

Desert shrubs are the dominant vegetation type in arid deserts and serve as crucial elements in sand retention, biodiversity maintenance, and carbon sequestration. However, due to their patchy and scattered distributions and spectral resemblance to herbaceous plants, desert shrub mapping relies on high-resolution imagery, which is less accessible for large-scale mapping. Here, a set of desert shrub mapping indices for Sentinel-2 ($DSMI_S$) and for universal medium-resolution imagery ($DSMI_L$) is developed to distinguish desert shrubs with dense vimen canopies. The index exploits the canopy structure and spectral characteristics, which have a sparse and multilayered canopy and a high proportion of desiccated branches, resulting in a consistently low reflectance in the red-edge to near-infrared range. The effectiveness of DSMI indices was examined in Ordos, China. In the experiment, an optimal threshold of 10.3 was obtained via DSMIs with Sentinel-2, which achieved an overall accuracy of 91.6% and identified a minimum desert shrub coverage of 0.23. In comparison, a threshold of 9.7 was obtained by $DSMI_L$ with Landsat-8, achieving an accuracy of 90.1% and identifying a minimum coverage of 0.17. The performance of DSMI was superior to that of the commonly used random forest, and this index could further improve classification as a complement to machine learning methods. The late stage of the nongrowing season was identified as the optimal period for desert shrub mapping with the index. DSMI also performed well at two test sites with diverse desert shrub dominant species and growing conditions. This study provides a novel index for desert shrub mapping and a practical tool for monitoring desertification in arid desert regions. It also offers a new perspective for historical dynamic studies of desert shrubs and other land cover types where only optical data are available.

ARTICLE HISTORY
Received 1 June 2024
Accepted 6 November 2024

KEYWORDS
Desert shrub; mapping; vimen canopy; DSMI; Sentinel-2

1. Introduction

Desert shrubs are perennial xerophytic shrubby vegetation growing in arid desert regions, which are also the dominant vegetation type in these regions (Feng et al. 2023; Mao et al. 2022). To adapt to the limited precipitation in deserts, desert shrubs have evolved fine leaves and extensive root systems (Feng et al. 2022; Gibbens et al. 2001). With inconspicuous stems and dense lateral branches, desert shrubs generally grow in clumps close to the ground. Thus, a conspicuous canopy of dense vimen, and fine foliage is the most distinctive morphological feature of desert shrubs (Figure 1). Desert shrubs play an important role in wind breaking and sand trapping through their dense branches and extensive root systems (Hu et al. 2021b). Desert shrubs also foster the development and maintenance of species diversity within desert ecosystems by increasing the soil moisture beneath their canopies, enriching soil nutrients, and regulating local microenvironmental temperatures (Hu et al. 2021a; Lan et al. 2021; Ward et al. 2018). Consequently, the mapping of desert shrubs is highly important for restoring desert ecosystems and controlling desertification.

Remote sensing has made large contributions to the acquisition of land surface information in recent decades because of its extensive coverage, rapid data acquisition, and periodic observations (Baumann et al. 2018; Brandt et al. 2016; Xun et al. 2021). Two primary sources of remote sensing data, namely optical and synthetic aperture radar (SAR) data, have been widely employed for shrub research. SAR has its own advantages, including the penetration of cloud and rain

CONTACT Bingfang Wu wubf@aircas.ac.cn
Supplemental data for this article can be accessed online at https://doi.org/10.1080/15481603.2024.2428366

© 2024 The Author(s). Published by Informa UK Limited, trading as Taylor & Francis Group.
This is an Open Access article distributed under the terms of the Creative Commons Attribution-NonCommercial License (http://creativecommons.org/licenses/by-nc/4.0/), which permits unrestricted non-commercial use, distribution, and reproduction in any medium, provided the original work is properly cited. The terms on which this article has been published allow the posting of the Accepted Manuscript in a repository by the author(s) or with their consent.

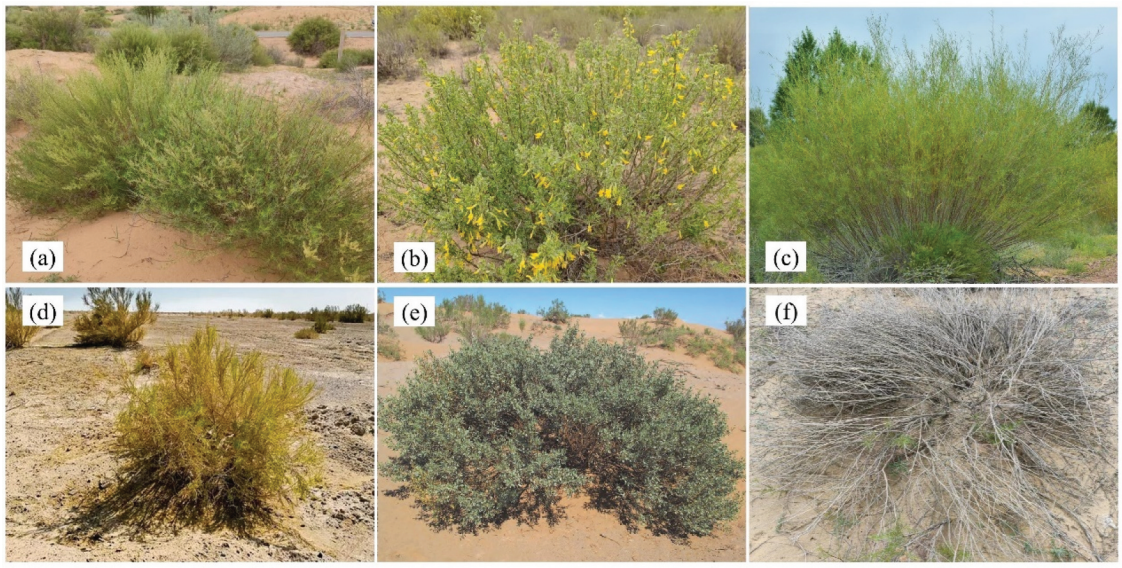


Figure 1. Various types of desert shrubs with canopies of dense vimen and fine foliage, including *Artemisia ordosica* (a), *Caragana korshinskii* (b), *Salix psammophila* (c), *Haloxylon ammodendron* (d), *Ammopiptanthus mongolicus* (e). The desiccated shrub (f), when the leaves have fallen but the branches remain, is also shown.

layers and the effective acquisition of canopy structure information (Baumann et al. 2018), which strongly supports studies of shrubs (Chang et al. 2017; Chang, Shoshany, and Oh 2018; Chang et al. 2022; Dąbrowska-Zielińska et al. 2012; Dabrowska-Zielinska et al. 2015). However, optical data remain the main data for Earth observations and surface parameter acquisition, especially in the historical period, when the SAR data were not fully developed and applied. The Landsat series, for example, provides the world's longest continuous Earth observation records and offers the most cost-effective and practical solution for large-scale mapping over a long time series (Zhang et al. 2024; Zhu et al. 2014). Sentinel-2 further enhances the potential application of optical data due to its high spatial resolution and short revisit periods (Wang et al. 2022), making it a better choice for desert shrub mapping. Therefore, the development of desert shrub identification methods based on optical data alone not only supports large-scale mapping of desert shrubs but also facilitates the investigation of historical dynamic changes.

Several methods have been applied to desert shrub mapping. Early studies focused primarily on desert shrub patch extraction through automatic algorithms and object-based segmentation techniques (Hellesen et al. 2013; Kopeć et al. 2020; Laliberte et al. 2004). The ability to mitigate speckling is the main advantage of these methods. However, these methods face challenges when applied to medium spatial resolution data (10–30 m), the primary data source for large-scale desert shrub mapping. Owing to their small size and scattered distribution, desert shrub patches often exist as mixed pixels in medium spatial resolution images. Classifier-based methods have also been widely employed for mapping land cover types, including shrublands (Baumann et al. 2018; Gong et al. 2013; Rüetschi et al. 2021; Zhang et al. 2021). Commonly used classifiers include support vector machine, random forest, and gradient boosting tree. These data-driven algorithms process high-dimensional feature and minimize the error between the predicted results and the actual samples, thereby improving the accuracy and efficiency of classification (Baumann et al. 2018; Chen et al. 2023a; Rüetschi et al. 2021). However, these approaches are typically considered black box models that lack transparency and interpretation, making the decision process difficult to understand (Chen et al. 2023b; Maxwell, Warner, and Fang 2018; Schulz, Hänsch, and Sörgel 2018). The models also perform weakly when learning from small sample sizes (Maxwell, Warner, and Fang 2018), meaning that model training relies on many samples to achieve a satisfactory result.

In contrast, index-based methods have recently attracted increasing attention in the identification of target objects, such as greenhouses, plastic materials,

sandy land, water bodies, artificial surfaces, and various crop types (Ashourloo et al. 2019; Ashourloo et al. 2020; Chen et al. 2021; Guo et al. 2020; Yang et al. 2017). The index-based method mines the universal characteristics of target objects, highlights these characteristics on remote sensing imagery through index construction, and then separates the target from background objects via a simple but practical threshold (Chen et al. 2023a; Xu et al. 2023; Xun et al. 2021). The method offers clear physical interpretations and reduces reliance on field samples while maintaining satisfactory performance (Chen et al. 2023a). Furthermore, indices typically represent continuous variables related to the coverage or probability of target objects (Xu et al. 2023), providing a more intuitive perception of spatial distribution and more flexible mapping. Therefore, developing a desert shrub mapping index with explicit physical meaning based on medium-resolution imagery appears to be a promising solution for large-scale desert shrub mapping.

However, the mapping of desert shrubs still faces several specific challenges when medium-resolution imagery is used as a data source. First, there is high spectral similarity between desert shrubs and herbaceous plants (Hellesen and Matikainen 2013), making it challenging to effectively differentiate them solely on the basis of spectral bands. Second, the issue of mixed pixels is prevalent in medium-resolution imagery (Mao et al. 2022). The sand-grass-shrub signal often blends within image pixels, which dilutes the distinct spectra of desert shrubs and mixes the redundant spectra from sand and grass. Consequently, the mapping accuracies for shrubs are not high in many mapping results (Chen et al. 2015; Gong et al. 2013; Zhang et al. 2021).

To address these challenges, extensive field trips were conducted to collect field samples, and a set of desert shrub mapping indices (DSMI) were proposed on the basis of medium-resolution imagery. Our study aims to (1) analyze the spectra of desert shrubs based on field spectra and satellite images (2); develop an effective index to facilitate the spatial mapping of desert shrubs on medium-resolution imagery (3); quantify the spatial distribution of desert shrubs and evaluate the performance of DSMI mapping; and (4) discuss the application of the DSMI in test regions and on Landsat imagery. To our knowledge, this is the first attempt to propose a practical index and achieve accurate and efficient desert shrub mapping from medium-resolution imagery. The index relies on optical data alone, which also provides a new perspective for historical dynamic studies of desert shrubs and other land cover types. This study not only lays the foundation for research on desert shrubs but also contributes to our understanding of desertification and assists in assessing desertification risk in arid regions.

2. Study area and data

2.1. Study area

The study area is located in Ordos (Figure 2, 37°35′24″–40°51′40″N, 106°42′40″–111°27′20″E), the central part of the Inner Mongolia Autonomous Region. The Ordos is located in the transition zone between the Mongolian-Siberian anticyclone high-pressure system and the southeast monsoon region (Teraminami et al. 2013), which is characterized by a warm temperate continental monsoon climate. The average annual temperature falls within the range of 5–8°C. Influenced by the maritime monsoon, the annual precipitation gradually decreases from east to west, typically ranging from 150 to 500 mm. Notably, annual evaporation rates range from 2000 to 2700 mm, surpassing the annual precipitation by 6–17 times. The study area occupies the transition zone between semi-arid and arid regions (Middleton et al. 1997)characterized by an ecological shift from steppe to desert steppe, steppe desert, and ultimately to desert. *Artemisia ordosica* and *Caragana korshinskii* are the dominant desert shrubs, accompanied by some herbaceous plants and scattered trees. The distributions of bare sand, sparse grassland, desert shrubs, and sparse forest form a unique vegetation pattern, making it an ideal study site for desert shrub identification.

Two additional study sites were also selected for validation: Alxa East County in Inner Mongolia and Bugur County in Xinjiang (Figure 2). Alxa East County, adjacent to Ordos, experiences a temperate continental climate characterized by abundant sunshine, scarce rainfall, and strong evaporation. The Tengger and Ulan Buh Deserts cross the region, making it more arid than Ordos. *Caragana korshinskii* and *Reaumuria soongarica* are the primary types of desert shrubs. Bugur County, located at the southern foot of the Tianshan Mountains, has a warm temperate continental arid climate. The average annual precipitation is only 52 mm, and the

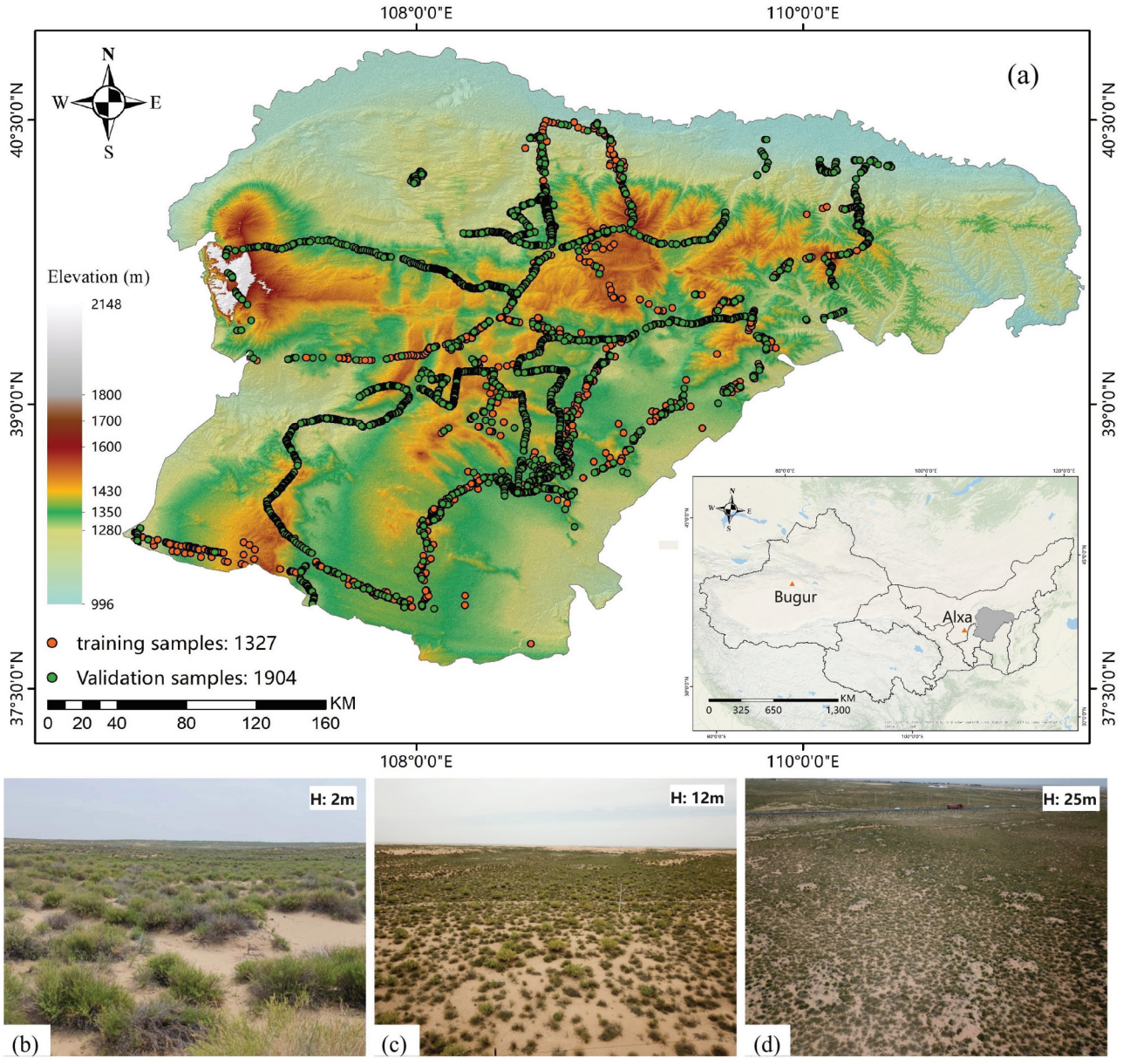


Figure 2. Locations of Ordos and two test sites (Orange triangles) and samples from field surveys (a), field photos of desert shrubs in typical plots taken with a hand-held camera (b) and drones (c, d). To indicate the size of the desert shrub patches, the heights of the sensors are labeled in the upper right corner of subfigure b, c, and d.

average annual evaporation is approximately 2077 mm. However, water resources are relatively abundant in this region because of the irrigation of several rivers, including the Tarim River. *Branchy tamarisk* is the primary desert shrub.

2.2. Data and preprocessing

2.2.1. Sentinel-2 images

Level-2A Sentinel-2 surface reflectance (SR) data sourced from the Google Earth Engine (GEE) (Gorelick et al. 2017) were employed to construct the index and identify desert shrubs. These SR data originate from the Sentinel-2 Multi-Spectral Instrument (MSI), a satellite instrument developed by the European Space Agency. The Level 2A products are generated through radiometric calibration, geometric correction, and atmospheric correction. These products encompass 13 spectral bands spanning from visible light to shortwave infrared with spatial resolutions ranging from 10 to 60 m. In the GEE platform, all the bands were resampled to 10 m

using the nearest neighbor method. In this study, 10 spectral bands (Table 1) and 12 spectral indices (Table 2) were selected as candidate features for DSMI design.

To avoid the potential noise introduced by cloud cover and shadows, all available SR images acquired throughout 2022 within Ordos were selected from GEE as the initial image dataset, with a requirement of cloud cover being below 30%. For each image in the dataset, the QA60 band containing cloud information was used to remove opaque, cirrus, and cloud shadows. Given the potential impact of pulsed rainfall events (Smith et al. 2019), the initial dataset was split into 20-day intervals. Synthetic image datasets with the same time intervals were generated by computing the median of all observations every 20 days, ensuring the consistency of the time intervals for each observation. Owing to cloud and cloud shadow masking, some pixels may not have sufficient high-quality observations. In such cases, linear interpolation was applied using high-quality observations from the previous and subsequent time steps to fill the gaps (Xun et al. 2021).

2.2.2. Training and validation samples

All training and validation samples in Ordos were derived from two field surveys. The first survey took place in July 2022, during which GVG software (https://gvgserver.cropwatch.com.cn/download) on mobile phones was used to mark land cover types and record their locations (Tian et al. 2004). The second survey was conducted in May 2023. A total of 1658 and 1573 valid samples were collected from the first and second surveys, respectively. All the sample points were ultimately classified into five categories according to the field survey, including bare sand, sparse grassland, desert shrub, sparse forest, and crops (predominantly maize). To avoid potential interference from different samples in model training and validation, 80% of the randomly selected samples from the first survey, which included 1327 points, were used as the training set. The remaining 20% of the samples, along with those collected in the second survey, constituted the validation set. A total of 1904 sample points were included in the validation sets (Figure 2).

For the two test sites, reference data were also collected from field surveys in April and May 2023.

Table 1. Spectral bands from Sentinel-2 used in this study.

Band	Band name	Central wavelength/nm	Spatial resolution/m	Abbreviation
B2	Blue	490	10	*blue*
B3	Green	560	10	*green*
B4	Red	665	10	*Red*
B5	Red edge1	705	20	*edge1*
B6	Red edge2	740	20	*edge2*
B7	Red edge3	783	20	*edge3*
B8	Nir	842	10	*nir*
B8A	Red edge4	865	20	*edge4*
B11	Swir1	1610	20	*swir1*
B12	Swir2	2190	20	*swir2*

Table 2. Spectral indices used in this study.

Spectral index	Abbreviation	Expression
Normalized difference vegetation index	NDVI	$\frac{nir-red}{nir+red}$
Enhanced vegetation index	EVI	$\frac{2.5*(nir-red)}{nir+6*red-7.5*blue+1}$
Green normalized difference vegetation index	GNDVI	$\frac{nir-green}{nir+green}$
Soil adjusted vegetation index	SAVI	$\frac{1.5*(nir-red)}{nir+red+0.5}$
Optimized soil adjusted vegetation index	OSAVI	$\frac{1.16*(nir-red)}{nir+red+0.16}$
Normalized difference greenness index	NDGI	$\frac{(0.6*green+0.38*nir)-red}{(0.6*green+0.38*nir)+red}$
Normalized difference moisture index	NDMI	$\frac{nir-swir1}{nir+swir1}$
Normalized difference phenology index	NDPI	$\frac{nir-(0.78*red+0.22*swir1)}{nir+(0.78*red+0.22*swir1)}$
Normalized difference residue index	NDRI	$\frac{red-swir2}{red+swir2}$
Normalized difference senescent vegetation index	NDSVI	$\frac{swir1-red}{swir1+red}$
Normalized difference tillage index	NDTI	$\frac{swir1-swir2}{swir1+swir2}$
Transformed normalized difference vegetation index	TNDVI	$\sqrt{\frac{nir-red}{nir+red}+0.5}$

Despite the short survey period at these two sites, some valid samples were still obtained. A total of 339 and 281 samples were collected in the test sites at Alxa East County and Bugur County, respectively.

2.2.3. In-situ spectral data

In May 2023, spectral measurements were carried out in Ordos. A FieldSpec 4 spectrometer (FS4N1500), manufactured by ASD Inc., was employed to measure and record the spectral reflectance of the desert shrubs and the surrounding land covers in typical plots. A handheld instrument was employed to obtain measurements at wavelength increments of 1 nm between 350 and 2500, with a 25° field of view, at a height of approximately 0.3 m above the surface feature, i.e. the desert shrub canopy. The spectral measurements were conducted between 10:00 and 14:00 local time under bright, clear, and sunny conditions. All the recorded spectra were converted to reflectance values via a white reference spectral panel. Noise bands caused by atmospheric water vapor absorption and sensor switches were removed in the ranges 1350–1450 nm, 1800–1999 nm, and 2401–2500 nm (Guo and Li 2020). To mitigate potential errors, five spectral curves were measured repeatedly for each land type, and the average was used as the final reflectance spectrum.

2.2.4. Land cover data

To eliminate interference from non-desert ecosystems, the land cover of Ordos was utilized to mask the satellite imagery, effectively excluding typical forest, grassland, cropland, wetland, and urban ecosystems. Only the spatial extent of desert ecosystems was retained as a potential growth area for desert shrubs. The land cover data employed were sourced from ChinaCover2020 provided by the Chinese Academy of Sciences (Wu et al. 2017). The overall accuracy for the first-level class exceeds 93.6%, and the accuracy for the second-level class exceeds 87.7%.

3. Methodology

3.1. Development of the DSMI

3.1.1. Ground spectra analysis

Figure 3 presents the reflectance spectra of common ground components. It demonstrates that the reflectance of the desert shrub canopy is significantly lower than that of the grass and sand in the red edge to near-infrared range, slightly lower than that of grass, and markedly lower than that of sand in the blue and green ranges. Specifically, in the visible light range, the reflectance depends mainly on the chlorophyll content and vegetation coverage (Zhang et al. 2006). Desert shrubs have evolved fine and whitish leaves to avoid overheating damage (Feng et al. 2022), resulting in a low canopy chlorophyll content and vegetation coverage. Furthermore, the sparse and multilayered canopy of desert shrubs, which consists of fine leaves and long vimen, not only reduces the leaf area index but also introduces many shadows, the presence of which leads to a further reduction in reflectance. Therefore, there is a slightly higher reflectance in the visible light range in the grass spectrum than desert shrub.

In the red edge to near-infrared range, noticeable spectral differences exist between desert shrubs and grasses. The reflectance of desert shrubs and grasses increases steeply in the red edge range and maintains high reflectance in the near-infrared range, which is largely influenced by the internal structure of the leaves (Knipling 1970). Despite the higher aboveground biomass of desert shrubs, the presence of desiccated shrubs in the canopy and the multilayered and sparse structure of the canopy still result in a lower reflectance of desert shrubs in the near-infrared region than that of grass. The reflectance of desiccated shrubs shows a slow and continuous increase without specific peaks or troughs in the visible light to near-infrared range, which is influenced mainly by lignin reflectance characteristics (Elvidge 1990). In the red edge to near-infrared range, the reflectance of desiccated shrubs is notably lower than that of grasses, and in the green and blue bands it is slightly lower. In the shortwave infrared range, both desert shrubs and grasses exhibit a significant decrease in reflectance due to leaf water absorption (Fensholt et al. 2003). Although the reflectance of desert shrubs is still lower than that of grass, the reflectance of desiccated shrubs is higher than that of grass.

Spectral measurements were also conducted on branches, leaves, and the canopy of desert shrubs in typical plots (Figure 3). There are high similarities in the spectral curves of desert shrub canopies and branches, both in shape and magnitude. This similarity was attributed primarily to the dense branches and small

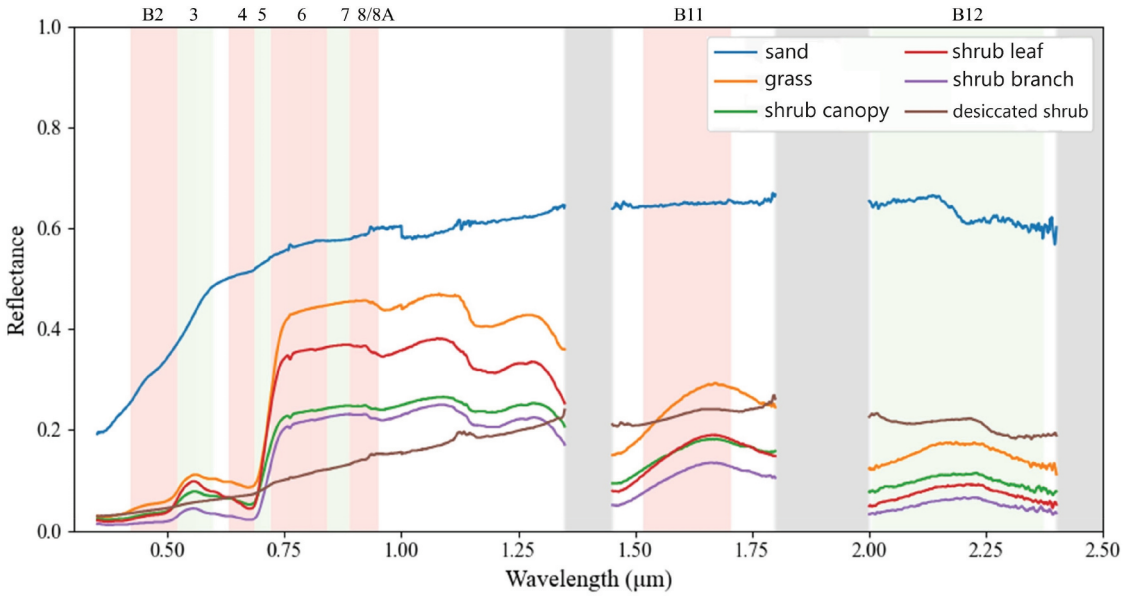


Figure 3. Reflectance spectra of common ground covers and different components of the desert shrub canopy in typical sample plots.

foliage of desert shrub canopies, leading to a more substantial influence from branches on the canopy spectra. Owing to the lower amplitude of the reflectance peak on desert shrub branches, the spectral peaks at 560 nm and 1665 nm wavelengths in the canopy did not exhibit the pronounced amplitudes observed for the leaves. Similarly, the canopy spectra of desert shrubs lacked large reflectance drops at the 970 nm and 1140 nm wavelengths, as observed in the leaves. Additionally, the reflectance of desert shrub canopies was markedly lower than that of leaves. This reduction in reflectance was due mainly to the intricate multilayer canopy structure of desert shrubs, which effectively decreases the incoming radiation reflected by the canopy through multiple scattering and absorption processes (Wang et al. 2015).

In summary, the spectra of desert shrub branches strongly affect the canopy spectra of desert shrubs, making them notably lower than those of grass in the red edge to near-infrared range. The presence of desiccated shrubs within the canopy and the multilayered structure of the canopy further reduce the reflectance and amplify the spectral differences in these spectral ranges. Consequently, the spectral bands of the near infrared and red edge become essential features for distinguishing desert shrubs from sparse grasslands.

3.1.2. *Image spectra analysis*

To ascertain the efficacy of the aforementioned spectral bands in differentiating desert shrubs in satellite imagery, we measured the separability between desert shrubs and other samples based on different spectral bands, spectral indices and their combinations. The M index and JM distance were adopted to quantify this separability. The M index is defined as the absolute value of the difference between two means normalized by the sum of their standard deviations, whereas the JM distance is an improvement of the Bhattacharya distance, normalized between 0 and 2 to facilitate comparison between datasets (Sen, Goswami, and Chakraborty 2019). These metrics have been widely used in the analysis of spectral separability (Guo and Li 2020; Xun et al. 2021; Yang et al. 2017). Taking the separability between desert shrubs and sparse grasslands in the NIR band as an example, the formulas are as follows:

$$M = \frac{|\mu_1 - \mu_2|}{\sigma_1 + \sigma_2} \tag{1}$$

$$JM = 2\left(1 - e^{-B}\right) \tag{2}$$

$$B = \frac{1}{8}(\mu_1 - \mu_2)^2 \frac{2}{\sigma_1^2 + \sigma_2^2} + \frac{1}{2}\ln\left(\frac{\sigma_1^2 + \sigma_2^2}{2\sigma_1\sigma_2}\right) \tag{3}$$

where μ_1 and μ_2 are the means of desert shrubs and sparse grasslands in the NIR band, respectively, and σ_1 and σ_2 are the standard deviations. It indicates good separability when the M index is greater than 1 or the JM distance is greater than 138 (Deng et al. 2012) and poor separability when the M index and JM distance are less than 1 (Xun et al. 2021).

Based on the training set, we obtained image spectra for bare sand, sparse grassland, desert shrub, sparse forest and crop. Separability analysis of these image spectra revealed high separability between desert shrubs and bare sand, as well as between desert shrubs and crops in all spectral bands (Figure S1), with average M indices of 2.31 and 1.64, respectively. However, the average M indices and JM distances between desert shrubs and sparse grasslands were only 1.17 and 1.00, respectively. Similarly, the average M indices and JM distances between desert shrubs and sparse forests only reached 0.90 and 0.79, respectively. Therefore, it is urgent to design sensitive features that can effectively discriminate desert shrubs from sparse grasslands and sparse forests.

Although high separability exists in the *edge2, edge3, edge4*, and *nir* bands (Figure S1), many desert shrub samples cannot be distinguished from sparse grasslands, with maximum M indices and JM distances of only 1.30 and 1.15, respectively. To further increase the spectral differences, addition and multiplication operations were performed on each pair of spectral bands. Compared with single band, addition and multiplication operations largely increased the spectral differences between desert shrubs and sparse grasslands, with addition (Figure 4) showing higher separability. The spectral separability in the addition results between *blue, green* and *edge2, edge3, edge4*, and *nir* is higher than that in other combinations. Through band addition, the top 2 maximum separability occurs with the addition of *blue* and *edge4* (aBlueEdge4) and the addition of *blue* and *nir* (aBlueNir), with M index values of 1.42 and 1.39, respectively. However, for sparse forests, higher separability with desert shrubs occurs in the *swir1* and *swir2* bands, and the band operations did not increase separability as so much. The maximum M indices and JM distances between desert shrubs and sparse forests reached only 1.10 and 0.94, respectively.

To separate sparse forests from desert shrubs, index values for different spectral indices for typical land cover types are obtained based on the training samples. Larger differences between desert shrubs and sparse forests are recorded in the spectral indices than in the spectral bands, with the M indices all above 1 (Figure S2). Figure 5 presents the M index and JM distance between desert shrub and non-desert shrub samples in these spectral indices, in which the digits from 0 to 4 indicate bare sand, sparse grassland, desert shrub, sparse forest and crop, respectively.

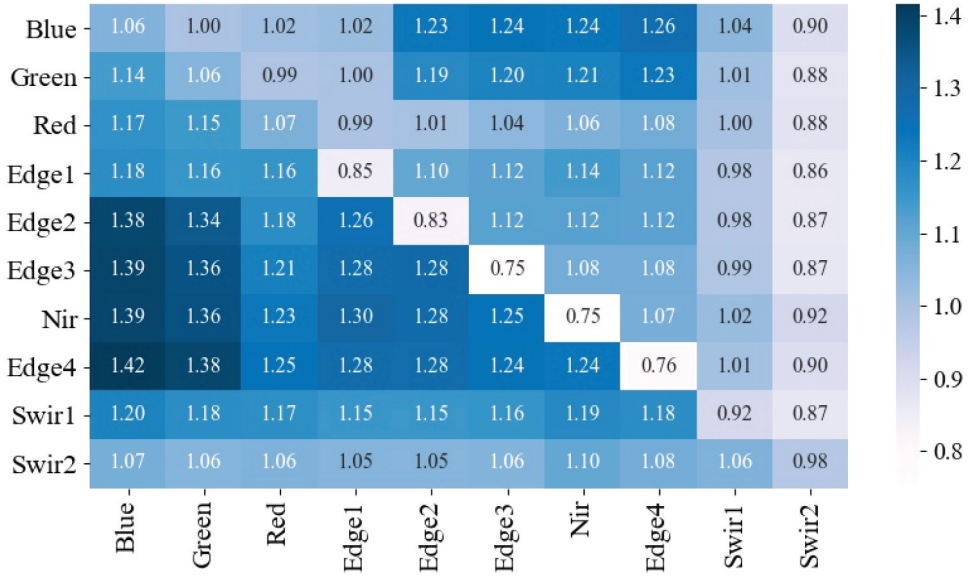


Figure 4. M-index values and JM distances between desert shrubs and sparse grasslands in the addition results for each pair of spectral bands. The lower left corner of the matrix shows the M-index values, and the upper right corner shows the JM distances. The elements on the diagonal are the average of the M-index.

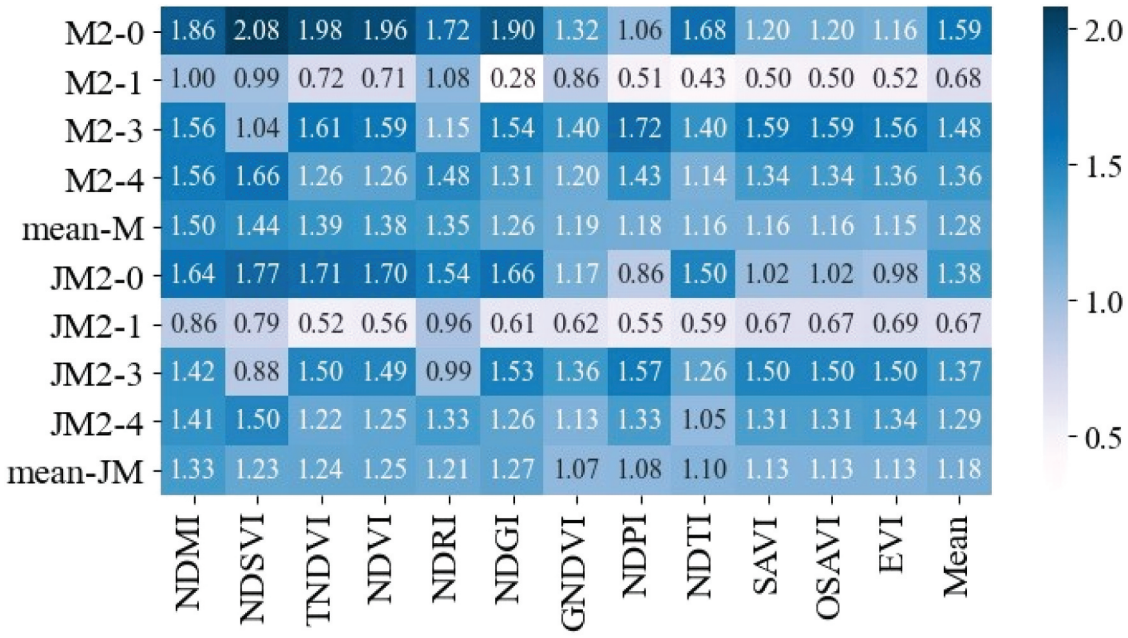


Figure 5. M-index and JM distance between desert shrubs and other samples (a) for different vegetation indices. The digits 0, 1, 2, 3, and 4 represent bare sand, sparse grassland, desert shrub, sparse forest, and crop, respectively.

Among these indices, the NDPI, TNDVI, OSAVI, SAVI, NDVI, NDMI and EVI maintained greater differences, with M indices all higher than 1.50. To obtain great differences between desert shrubs and sparse forests and maintain high separability between desert shrubs and other non-desert shrub samples, the NDMI index was selected, as it has a higher mean M-index (1.50) and JM distance (1.33) between desert shrubs and non-desert shrubs (Figure 5). Another reason for the selection of the NDMI is that the NDMI encompasses moderate separability between sparse grasslands and desert shrubs, with an M-index of 1.00, which is only slightly lower than the NDRI of 1.08.

For sparse forest, *swir1, swir2* and NDMI had higher separability. In fact, all these features reflect to some extent the canopy water content (Klemas et al. 1983) for desert shrubs and sparse forests, with the NDMI performing better. As natural vegetation in desert regions, both desert shrubs and sparse forests suffer from water shortages. However, compared with desert shrubs, sparse forests typically grow in areas with more water supply, such as along rivers and near wetlands. Thus, sparse forests usually have higher leaf moisture contents than desert shrubs. As a result, the NDMI can better distinguish desert shrubs from sparse forests.

3.1.3. Construction of the DSMI

For the sensitive features aBlueEdge4 and aBlueNir, both desert shrubs and sparse forests presented the lowest feature values, which were significantly lower than those of sparse grasslands, crops, and bare sand (Figure 6). Through band addition operations, these sensitive features were used to further enhance the spectral distinctions between desert shrubs and sparse grasslands. Specifically, the M index increased from 1.23 to 1.42, and the JM distance rose from 1.07 to 1.27. In terms of the sensitive feature NDMI, the feature values of desert shrubs were notably lower than those of sparse forests and slightly lower than those of sparse grasslands, bare sand, and crops. For the NDMI, desert shrubs not only presented profound differences from sparse forests but also presented moderate disparities from sparse grasslands, with an M index of 1.00.

Considering the spectral distribution of sensitive features, the DSMI is proposed. The $DSMI_S$ is a composite index with reflectance bands of Blue, Red Edge4 from Sentinel-2 and NDMI. Moreover, owing to the high similarity in spectral distribution between aBlueEdge4 and aBlueNir (Figure 6), substituting aBlueEdge4 with aBlueNir not only preserves the effectiveness of the DSMI index but also enhances its applicability to other satellite data that lack red-edge bands, such as Landsat. Therefore, we substitute

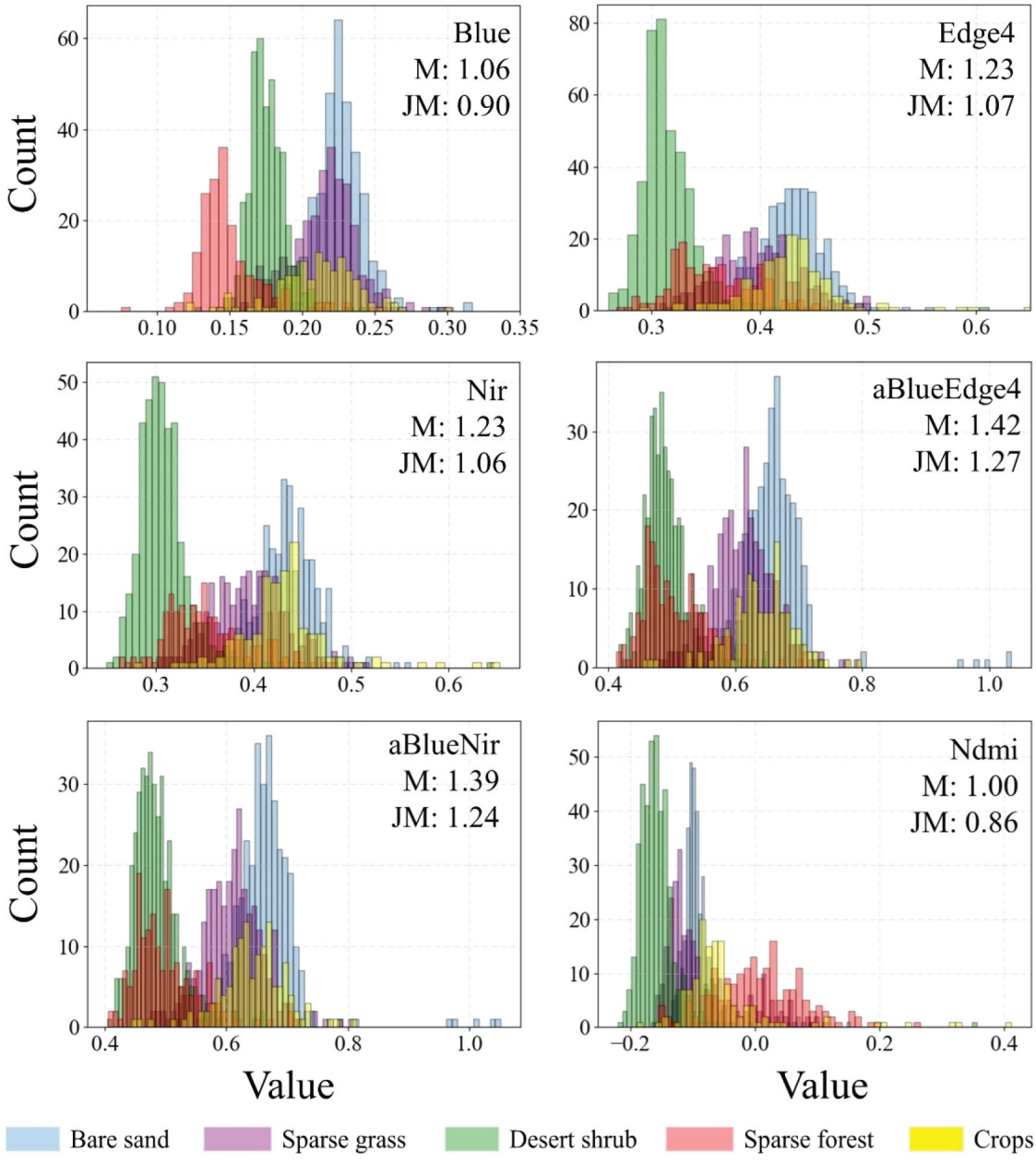


Figure 6. Histogram of sensitive features for typical surface components. The M-index and JM distance indicate the separability index between desert shrubs and sparse grasslands.

the *edge*4 band with *nir* and construct the $DSMI_L$ index. This adaptation ensures the versatility of the index across different satellite sensors.

$$DSMI_S = \frac{(2 - blue - edge4)}{(blue + edge4) * (NDMI + 0.4)} \quad (4)$$

$$DSMI_L = \frac{(2 - blue - nir)}{(blue + nir) * (NDMI + 0.4)} \quad (5)$$

To verify the difference in DSMI indices between desert shrubs and non-desert shrubs, we plotted a scatterplot based on their DSMI values (Figure 7). The $DSMI_S$ and $DSMI_L$ values for desert shrubs are clearly higher than the others. The mean $DSMI_S$ values for desert shrubs, sparse grasslands, sparse forests, bare sand, and crops are 13.1, 7.3, 7.4, 6.7, and 6.2, respectively. The M indices (JM distances) between desert shrubs and non-desert shrubs on $DSMI_S$ and $DSMI_L$ are 181 (1.60) and 179 (1.59), respectively. Furthermore, all the samples are distributed along a straight line with a slope of 1.0, indicating that the $DSMI_S$ and $DSMI_L$ values are close to

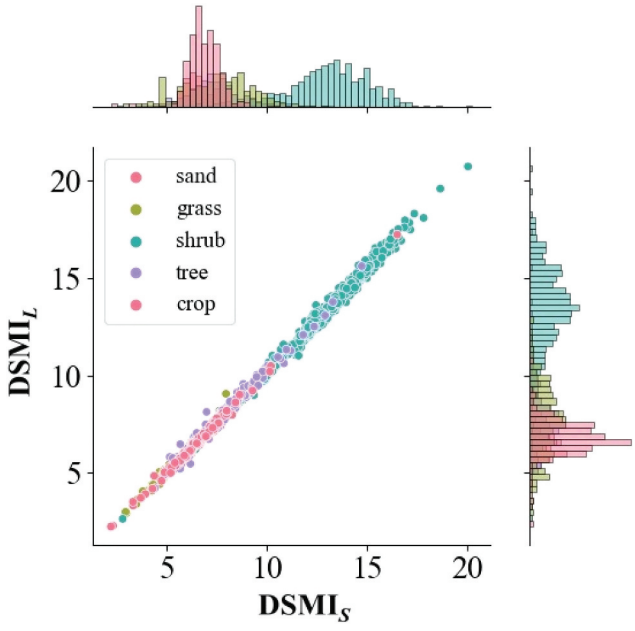


Figure 7. Scatter plots for different surface components in the $DSMI_S$-$DSMI_L$ feature space. Histograms of $DSMI_S$ and $DSMI_L$ values for different surface components are also presented.

each other, therefore replacing the *edge4* band with *nir* to improve the applicability of the index is reasonable.

corresponding to a better balance between the UA and PA was selected.

The DSMI value largely depends on the percentage coverage of desert shrubs within a certain extent. Hence, there exists a lower coverage limit that corresponds to the optimal threshold. If the desert shrub coverage within a pixel falls below this limit, the desert shrub signal will be overshadowed by other spectral signals and may not be detectable by the DSMI threshold. In this study, following the approach described by Chen et al. (2005), a pixel-based simulation process was implemented. According to the conditions of the study site, a mixed pixel was assumed to consist of three components: grass, bare sand and desert shrubs. These three components follow a linear spectral mixing model (Adams, Smith, and Johnson 1986), as shown in the equation.

$$\begin{cases} R_1(\lambda) = f_g \times R_g(\lambda) + f_s \times R_s(\lambda), \\ R_{mix}(\lambda) = f_1 \times R_1(\lambda) + f_d \times R_d(\lambda), \end{cases} \quad \begin{matrix} f_g + f_s = 1, f_g = 0, 0.1, 0.2, \ldots, 1.0 \\ f_1 + f_d = 1, f_d = 0, 0.1, 0.2, \ldots, 1.0 \end{matrix} \tag{6}$$

where R_1 represents the mixed spectra of grass and bare sand and f_g and f_s represent the fractions of grass R_g and bare sand R_s, respectively. R_{mix} represent the mixed spectra of desert shrubs R_d and R_1, whereas f_1 and f_d represent the fractions of R_1 and R_d, respectively. λ is the wavelength. The spectra of sand, grass, and desert shrubs are all derived from satellite imagery (Wang et al. 2022) based on pure pixels in each land cover type.

3.2. Application of the DSMI

The proposed DSMI was used in the extraction of desert shrubs in Ordos via an index-based method (Chen et al. 2023a; Xu et al. 2023). Prior to mapping, two crucial tasks needed to be addressed. First, the optimal segmentation threshold for DSMI mapping needed to be determined. Second, the lower bound of desert shrub coverage corresponding to the threshold has also to be determined.

A method for balancing the error between commission and omission was used to determine the optimal threshold (Ashourloo et al. 2020; Xun et al. 2021). With the training set, the accuracy for different thresholds was calculated with a step of 0.1. By examining the changes in User's Accuracy (UA), Producer's Accuracy (PA), Overall Accuracy (OA), Kappa, and F1-score, the threshold

3.3. Accuracy assessment

The independent validation set and confusion matrix were used to evaluate the accuracy of the proposed DSMI index. OA, UA, PA, and kappa were all calculated from the confusion matrix. The OA reflects the proportion of correctly classified validation sample points, the UA and PA represent the proportions of commissions and omissions, respectively, and the kappa indicates the agreement between the classification results and the reference results (Xun et al. 2021). In addition, the F1-score is

calculated from the UA and PA via the following equation:

$$F1 - score = 2 * \frac{UA * PA}{UA + PA} \quad (7)$$

The Random Forest (RF) classifier, a commonly utilized machine learning algorithm for land cover classification (Chen et al. 2023a; Wang et al. 2022), was employed as the comparative method. RF, as an ensemble classifier, generates multiple training subsets by randomly selecting a subset of samples. For each training subset, many decision trees are constructed, and the final classification result is determined by majority voting. RF mitigates the correlation between trained decision trees through the bagging algorithm, effectively alleviating overfitting problems (Tian et al. 2019). To assess the performance of the DSMI, we compared the classification results of the DSMI with those of the RF algorithm. In the RF classifier, a total of 12 spectral indices from Table 2 were input as initial features. Two key parameters of the RF classifier, including the number of trees and the number of predictor variables, were set to 500 and the square root of the number of input variables, respectively.

Furthermore, to demonstrate the importance of the DSMI in desert shrub mapping compared with the existing indices, a SHAP framework was used to obtain the feature importance from the RF classifier. SHAP is a game theoretic framework for explaining machine learning models (Lundberg et al. 2017). The framework treats each feature variable as a player and the results predicted by the model as the proceeds of a project completed through the cooperation of many players. The benefits of cooperation are distributed fairly by considering the contributions made by each player.

4. Results

4.1. Time windows for DSMI mapping

The temporal variation in the DSMI values for different land covers and the M index values between desert shrubs and non-desert shrubs were analyzed. During the nongrowing season (November to May of the second year), the DSMI values for bare sand, sparse grassland, sparse forest, and crops were close and lower than those for desert shrubs (Figure 8). The M indices also remained higher than 1.0 throughout this period. Upon entering the growing season (June–October), the DSMI values of desert shrubs decreased rapidly, becoming less distinguishable from those of sparse grasslands, sparse forests and crops. Two windows are identified as more suitable for DSMI mapping during the nongrowing season. The first window extends from November to December, whereas the second extends from March to June. Since the first window may be subject to snow cover, the second window is therefore more suitable for desert shrub

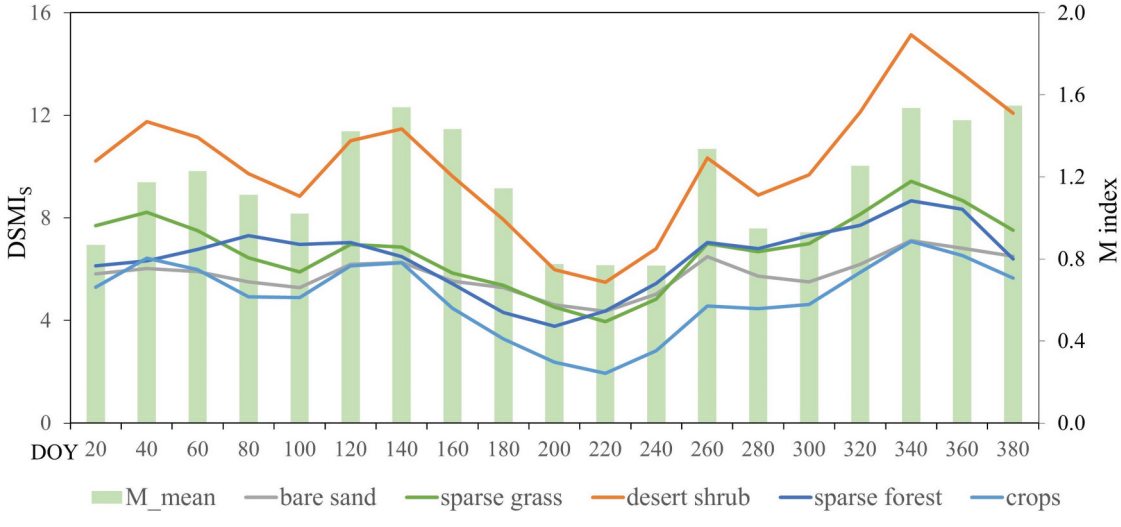


Figure 8. Temporal variation in DSMI values for common land cover types and the average M index between desert shrubs and non-desert shrubs. The DSMI values for desert shrubs remain significantly higher than those for other covers during the nongrowing season.

mapping. The second window also has a longer temporal extent.

This phenomenon is explainable. During the growing season, desert shrubs exhibit vegetative characteristics with strong spectral similarities to those of herbaceous plants. In particular, following an episodic precipitation event, the recovery of desert shrub foliage and the growth of sparse grassland increase the proportion of green components in mixed pixels, leading to a decrease in the DSMI. However, during the long nongrowing season, the proportion of dry branches in the canopy gradually increases as the leaves gradually wilt and wither due to lack of timely water supply. Compared to the background elements, the remaining dry branches exhibit large spectral differences because desiccated desert shrubs have lower reflectance in the red edge and near-infrared bands, lower NDMI values and therefore higher DSMI values.

4.2. Determination of the DSMI threshold

As depicted in Figure 9a, the OA, kappa, and F1-score initially increased but then decreased as the threshold increased. At lower thresholds, the omission error was minimal because the higher DSMI values of desert shrubs result in a higher PA. However, this led to a higher commission error and a lower UA. As the threshold increased, limited desert shrub samples with lower DSMI values were not accurately identified, but most non-desert shrub samples were correctly excluded, resulting in a gradual decrease in the PA and a rapid increase in the UA. In our study, setting the threshold to 10.3 achieved a balanced trade-off between commission and omission errors, with both the UA and PA reaching 0.92. This threshold corresponds to an OA of 0.96, a kappa of 0.90, and an F1-score of 0.92. However, at a threshold of 10.6, the classification attained the highest F1 score, with the UA surpassing the PA (0.94 vs. 0.91). The first threshold of 10.3 was adopted in this study to optimize the balance between commission and omission errors.

The DSMI values for various coverage scenarios are presented in Figure 9b. Across all the scenarios, the DSMI increased with increasing desert shrub coverage, as desert shrubs presented higher DSMI values than bare sand and grassland. When grass coverage increased, the non-photosynthetic component of grass introduced some variation in the DSMI value, contributing to the increase from 7.1 to 8.8 when desert shrub coverage was zero. Consequently, there was high uncertainty in the DSMI within this range, as it was influenced by both the spectral signals from desert shrubs and the non-photosynthetic component of sparse grassland and bare sand. Furthermore, with the DSMI threshold set at 10.3, the corresponding desert shrub coverage ranged from 0.23 to 0.45, increasing with increasing grass coverage. Hence, the adopted DSMI threshold detected desert shrubs with a minimum coverage of 0.23.

4.3. DSMI mapping result

The spatial distribution of desert shrubs was determined through the DSMI (Figure 10). By calculating the number of pixels, the total area covered by desert shrubs in Ordos is approximately 21,005 km^2, accounting for 24.2% of the total area. As shown in Figure 10, desert shrubs are widely distributed in the eastern and central parts of Ordos. The Mu Us Sandy Land to the southeast, the Kubuqi Desert to the north, and the Loess Hills to the northeast of the Ordos are the three hotspots for desert shrub growth. Soil moisture and terrain are the primary factors influencing the spatial distribution of desert shrubs. The average surface soil moisture in Figure 10b is derived from Song et al. (2022) and provided by the National Tibetan Plateau/Third Pole Environment Data Center (https://data.tpdc.ac.cn). The Loess Hills region, situated in the northeastern part of the study area and on the edge of the Loess Plateau, has higher soil moisture (Figure 10b). This results in a denser distribution of desert shrubs. However, the fragmented terrain and numerous gullies in this area also contribute to the fragmented distribution of desert shrubs. In the southeastern Mu Us, sand dunes, sparse grassland, and desert shrubs coexist. As soil moisture decreases, the desert shrubs in Mu Us gradually give way to sparse grassland and dunes, because the latter require less water to survive in the desert. The Kubuqi Desert experiences a dry and cold climate with strong winds, resulting in higher

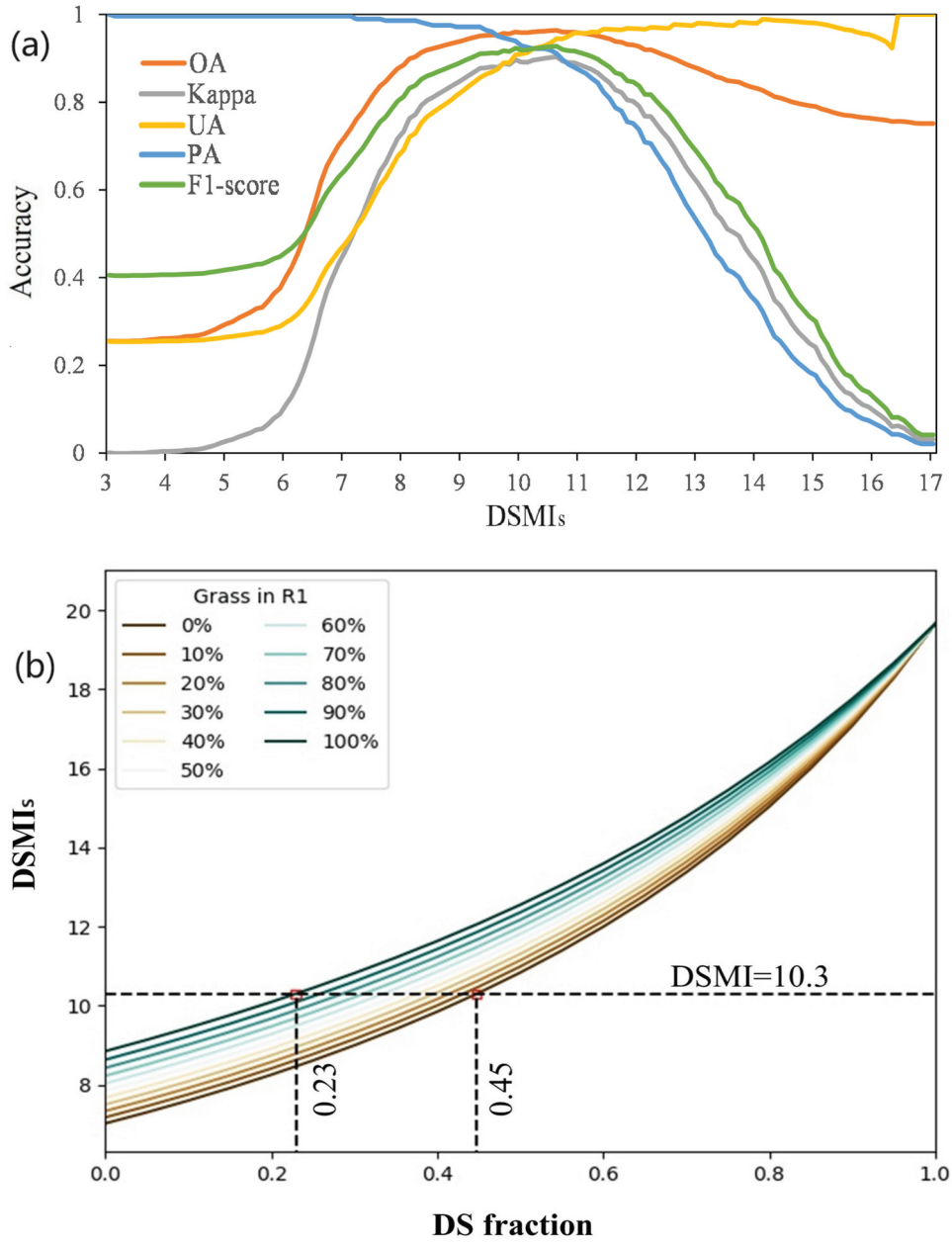


Figure 9. DSMI thresholds for desert shrub mapping in Ordos (a) and DSMI values in simulated scenarios with different desert shrub fractions (b). R1 indicates the mixed spectra of grass and bare sand, and DS indicates desert shrubs.

evapotranspiration than the Mu Us Desert. Limited soil moisture in Kubuqi also hinders the growth of desert shrubs, restricting their distribution to transitional areas on the eastern and southern edges of the desert. In the northwestern part of Ordos, the surface soil moisture continues to decrease, making it difficult to support the growth of desert shrubs. However, in the southwestern part of Ordos, localized distribution of desert shrubs is still observed due to its proximity to the Yellow River irrigation area in Ningxia.

4.4. Accuracy assessment of the DSMI results

Visual evaluation provides an intuitive analysis of the ability of DSMI to highlight desert shrubs. In the DSMI image, the DSMI values of desert shrubs are notably higher, shown in deep yellow to red color (Figure 11), whereas the index values of sand are low, shown in blue. The index values of sparse grassland fall between the two values, shown in blue to light yellow. Owing to the invasion of woody shrubs into sparse grasslands, the index values of sparse grasslands increased, as shown in light yellow.

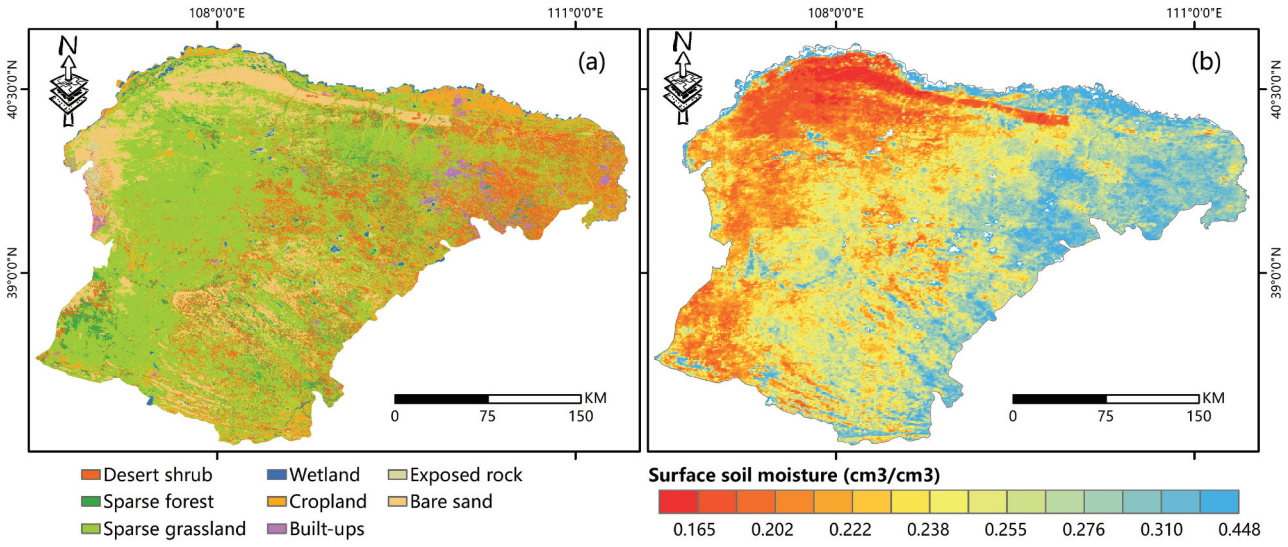


Figure 10. Classification results of desert shrubs (a) based on the optimal threshold of $DSMI_S$ and average surface soil moisture (b). Desert shrubs tend to grow in areas with higher soil moisture, such as the Loess Hills region in the northeast, the Mu Us in the southeast, and the eastern and southern edges of the Kubuqi Desert.

To evaluate the performance of the DSMI for different land cover types, true-color and DSMI images of typical plots were selected for comparison. The first plot comprises an interlaced distribution of bare sand, desert shrubs, and saline-alkali land. In the true-color image, bare sand, desert shrubs, and saline-alkali land are presented in yellow, brown, and white, respectively (Figure 11b). In the DSMI image, bare sand and saline-alkali land are displayed in light blue and dark blue, respectively (Figure 11e). The index values of the desert shrubs are clearly higher than the former two, as shown in yellow and red. The second plot contained non-invaded and invaded sparse grassland by desert shrubs (Figure 11c–f). The noninvaded sparse grassland appears slightly green in the true-color image and light blue in the DSMI image, whereas the invaded sparse grassland appears slightly brown in the true-color image and light yellow in the DSMI image. The third plot includes cultivated land and built-up areas, which appear in dark blue and light blue, respectively, in the DSMI image (Figure 11d–g).

To quantify the mapping accuracy, independent validation samples and a confusion matrix were used (Table 3). The results show that the DSMI has a high discriminatory ability for both desert shrub and non-desert shrub samples, with an overall accuracy of 91.6%. The corresponding F1-score and kappa value are 0.90 and 0.83, respectively. For desert shrubs, the UA is slightly higher than the PA (0.94 vs. 0.86), indicating a higher overlooked error. Although there is a slight underestimation of desert shrubs in the results, both the UA and PA are above 0.85, indicating that the errors of commission and omission are acceptable.

Compared with the RF method, the DSMI method shows an advantage. The Kappa, F1-score, and OA improved by 3%, 2%, and 1.1%, respectively, indicating that the DSMI method achieved a comparable and even better performance than the random forest method. However, the high accuracy of RF is based on 12 spectral indices and complex machine learning, whereas the DSMI method relies on only a single Sentinel-2 image and a binary classification threshold. Notably, the DSMI method demonstrates the smaller difference between the UA and PA in identifying desert shrubs, indicating that the DSMI achieves a more balanced trade-off between omission and commission errors. Furthermore, by replacing the most important features with the DSMI, the accuracy could be further improved, with an OA of 0.923 and kappa of 0.84. It also implies that the DSMI provides more contribution to desert shrub identification than existing indices do.

Furthermore, as shown in Figure 12, the spectral indices are ranked in descending order according to their mean absolute values of the SHAP values. The results show that both $DSMI_S$ and $DSMI_L$ have higher contributions than existing spectral indices. Notably,

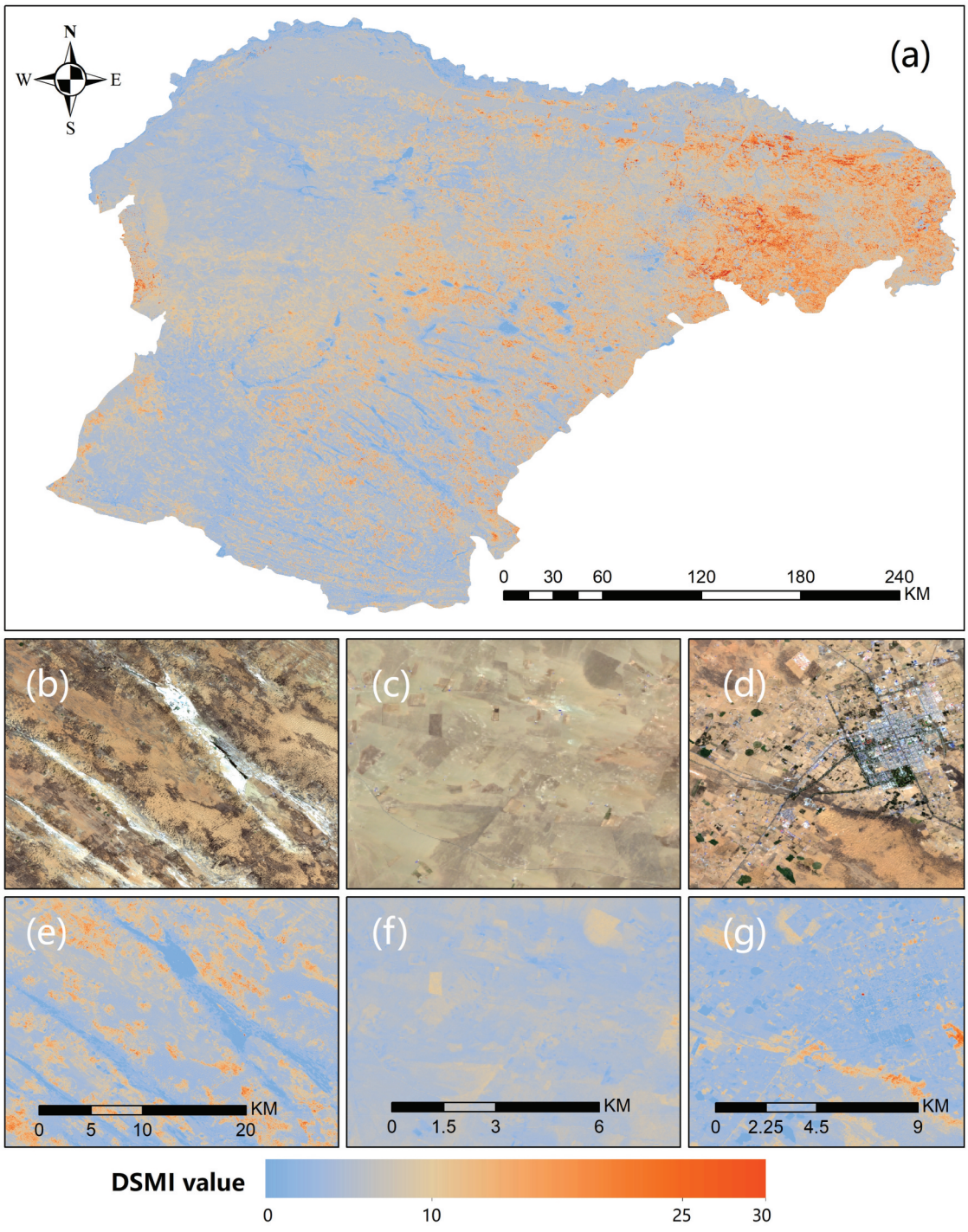


Figure 11. DSMI image for the whole study area (a) and true color images for three typical plots (b, c, d) and the corresponding DSMI images (e, f, g).

the SHAP values of both $DSMI_S$ and $DSMI_L$ demonstrate a wide distribution with two clusters, where the blue cluster indicates a lower DSMI value and a lower probability of desert shrubs. The red cluster indicates a higher DSMI value and a higher probability of desert shrubs. In contrast, the distribution pattern of the NDMI appears to be less distinct than that of the DSMI, with red scatter points and small blue scatter points in the range of SHAP values less than 0. This suggests that a low NDMI value might introduce ambiguity in the classification of desert shrubs, as it may exert a positive or negative impact on the model output. A similar pattern is also observed for the NDRI.

Table 3. Confusion matrix and accuracy metrics for the classification results of the two methods. DS indicates desert shrubs. DSMI-RF means replacing the most important feature with DSMI.

Method	Confusion matrix	Non-DS	DS	PA	OA	Kappa	F1-score
DSMI	Non-DS	1048	44	0.96	0.916	0.83	0.90
	DS	116	696	0.86			
	UA	0.90	0.94				
RF	non-DS	1050	42	0.96	0.905	0.80	0.88
	DS	138	674	0.83			
	UA	0.88	0.94				
DSMI-RF	non-DS	1066	26	0.97	0.923	0.84	0.90
	DS	121	691	0.85			
	UA	0.90	0.96				

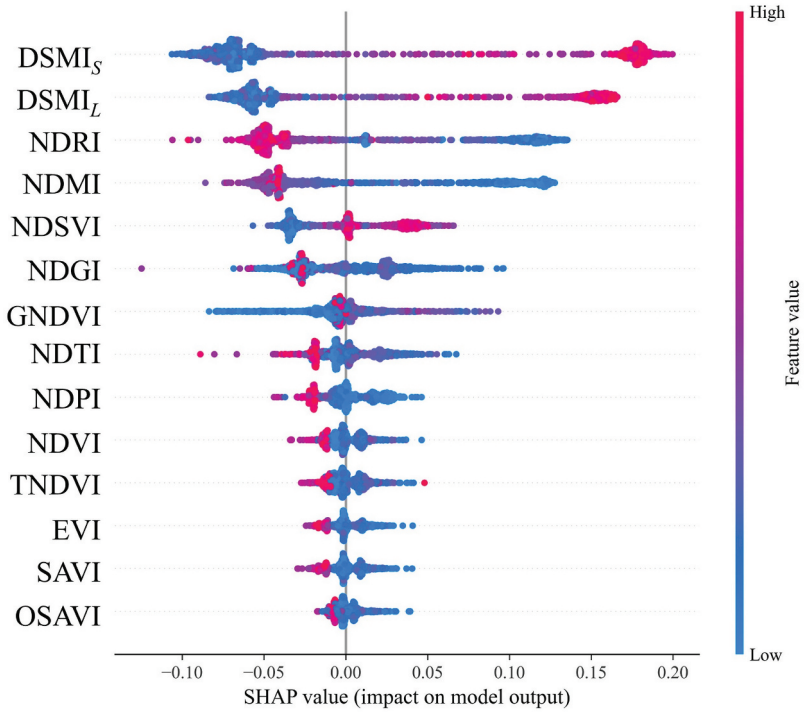


Figure 12. Feature importance analysis based on SHAP for RF.

5. Discussions

5.1. DSMI generalization in Landsat-8 images

To evaluate the applicability of the DSMI to other medium-resolution satellite data, we experiment with surface reflectance imagery from Landsat-8 OLI. To harmonize the surface reflectance between Landsat-8 OLI and Sentinel-2 MSI, an ordinary least squares linear regression method described by Cao, Han, and Li (2022) was used to convert the Landsat-8 reflectance values closer to the Sentinel-2 values. Since Landsat-8 imagery lacks the RE4 band, we used the NIR band instead to calculate the DSMI$_L$ results. Figure 13a displays the DSMI$_L$ results calculated using the Landsat-8 OLI composite image, revealing that the spatial distribution of desert shrubs from Landsat-8 OLI aligns with that from the Sentinel-2 image (Figure 10). This map effectively highlights the spatial distribution of desert shrubs through the DSMI$_L$ index, making them easily distinguishable from other land covers. The frequency distribution of DSMI$_L$ values for different land covers on Landsat-8 images is also illustrated in Figure 13b, which shows that the DSMI$_L$ values for desert shrubs are consistently higher than those for non-desert shrubs, with an M-index and JM distance of 1.40 and 1.26, respectively. These findings underscore the robustness of the DSMI on Landsat-8 imagery and reveal its potential for large-

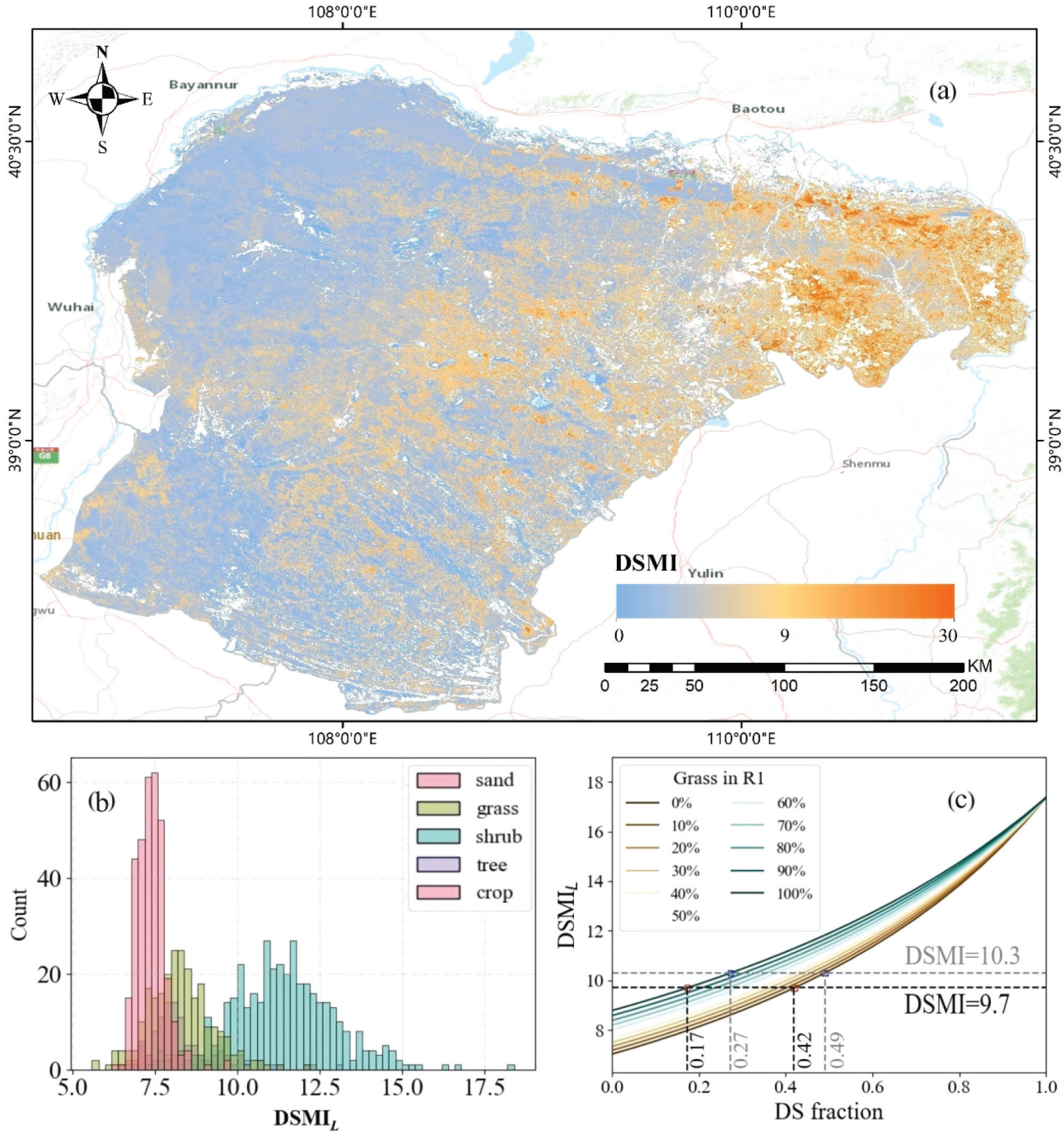


Figure 13. Spatial distributions (a) and histograms (b) of the DSMI$_L$ values and simulated scenarios with different desert shrub fractions (c) in the Landsat-8 OLI image.

scale mapping of desert shrubs via satellite data from the longest continuous Earth observation record.

Based on the training samples and Landsat-8 images, the optimal threshold for Landsat-8 images was determined to be 9.7, which is 0.6 lower than that for Sentinel-2 images. With a threshold of 9.7, the accuracy of the DSMI$_L$ classification results was assessed with the validation samples, yielding an OA of 90.1% and an F1-Score of 088 (Table 4). The decrease in spatial resolution is responsible for the decrease in the optimal threshold. Since it is difficult to sustain a large-area and continuous coverage of desert shrubs in arid desert regions, for samples labeled desert shrubs, a 30-m resolution contains

Table 4. Desert shrub/non-desert shrub confusion matrix based on the validation samples.

	Desert shrub	Non-desert shrub	Total
Desert shrub	677	135	812
Non-desert shrub	54	1038	1092
Total	731	1173	1904

OA: 90.1%, Kappa:0.79, UA: 0.93, PA: 0.83, F1-Score: 0.88, threshold: 9.7.

more spectra from bare sand and sparse grass, reducing the pixel values of $DSMI_L$ and resulting in a lower segmentation threshold. Consequently, it also results in a reduction in the minimum detectable desert shrub coverage. As shown in Figure 13c, the threshold of 9.7 corresponds to desert shrub coverage ranging from 0.17 to 0.42 in the Landsat-8 image. Although the minimum detectable desert shrub coverage is approximately 0.17 and lower than the minimum coverage for Sentinel-2, this does not indicate that the Landsat-8 sensor has higher recognition of desert shrubs than Sentinel-2. To provide a more objective evaluation of desert shrub recognition between Landsat-8 and Sentinel-2, we simulated the range of desert shrub coverage detected by both sensors under the same segmentation threshold. The results show that the minimum desert shrub coverage of the 10.3 threshold is approximately 0.27 for Landsat-8 imagery, which is higher than that for Sentinel-2 imagery. Thus, higher spatial resolution contributes to more accurate detection of low coverage and small desert shrub patches. However, a higher resolution may also increase the amount of intrusive noise in the images, leading to misclassification of desert shrubs with greater spectral variability and reducing the classification accuracy. Moreover, the scale effect also suggests that appropriate resolution helps to better understand geographical phenomena.

5.2. DSMI generalization at test sites

To evaluate the effectiveness of the DSMI in diverse arid desert regions, we conducted a validation of desert shrub extraction in Alxa East County, Inner Mongolia, and Bugur County, Xinjiang. The results revealed high accuracy in both regions. The OA and F1-score in Alxa East County were 0.92 and 0.90, respectively, whereas those in Bugur County were both 090 (Table 5). In terms of desert shrubs, the UA was slightly lower at both sites, indicating a slightly higher misclassification error. In contrast, the PA values for non-desert shrubs were lower at both sites, indicating slightly higher overlooked errors. This suggests a slight overestimation of desert shrubs in the classification result. In either case, despite the limited number of training samples, DSMI consistently yielded satisfactory extraction results (Figure 14).

However, the optimal segmentation threshold of the index varied, decreasing to 8.6 in Alxa East County and to 6.3 in Bugur County (Table 5). We attribute these variations to the differences in the type and growth conditions of desert shrubs. Owing to variances in the canopy spectra and canopy structure of different desert shrubs, as well as varying proportions of desiccated shrubs in the community, the response of the index to the spectral signal varied by region. In Ordos, *Artemisia ordosica* and *Caragana korshinskii* are the dominant desert shrub types. However, the desert shrubs at the test site in Alxa East County are dominated by *Caragana korshinskii* and *Reaumuria soongarica*, whereas the desert shrubs at the test site in Bugur County are dominated by *branchy tamarisk*. The variability of desert shrub types in different regions may be the essential reason for the variation in index thresholds. The growth conditions of desert shrubs could also affect the threshold. During the field survey, we found that Alxa East County is drier than Ordos, and desert shrubs' growth condition is worse. Most desert shrubs are found in clumps on the ground, with sparse leaves and branches in the canopy. This leads to a mixture of canopy spectra with bare sand spectra, resulting in lower DSMI values for desert shrubs. However, irrigation from the Tarim River resulted in a higher leaf area index and greener

Table 5. Accuracy assessment at the two test sites, based on validation data. DS indicates desert shrubs.

	Confusion matrix						
Region		DS	Non-DS	PA	OA	Kappa	F1-score
Alax East County	DS	37	2	0.95	0.92	0.84	0.90
	Non-DS	6	57	0.90			
	UA	0.86	0.97				
Bugur County	DS	36	2	0.95	0.90	0.81	0.90
	Non-DS	6	40	0.87			
	UA	0.86	0.95				

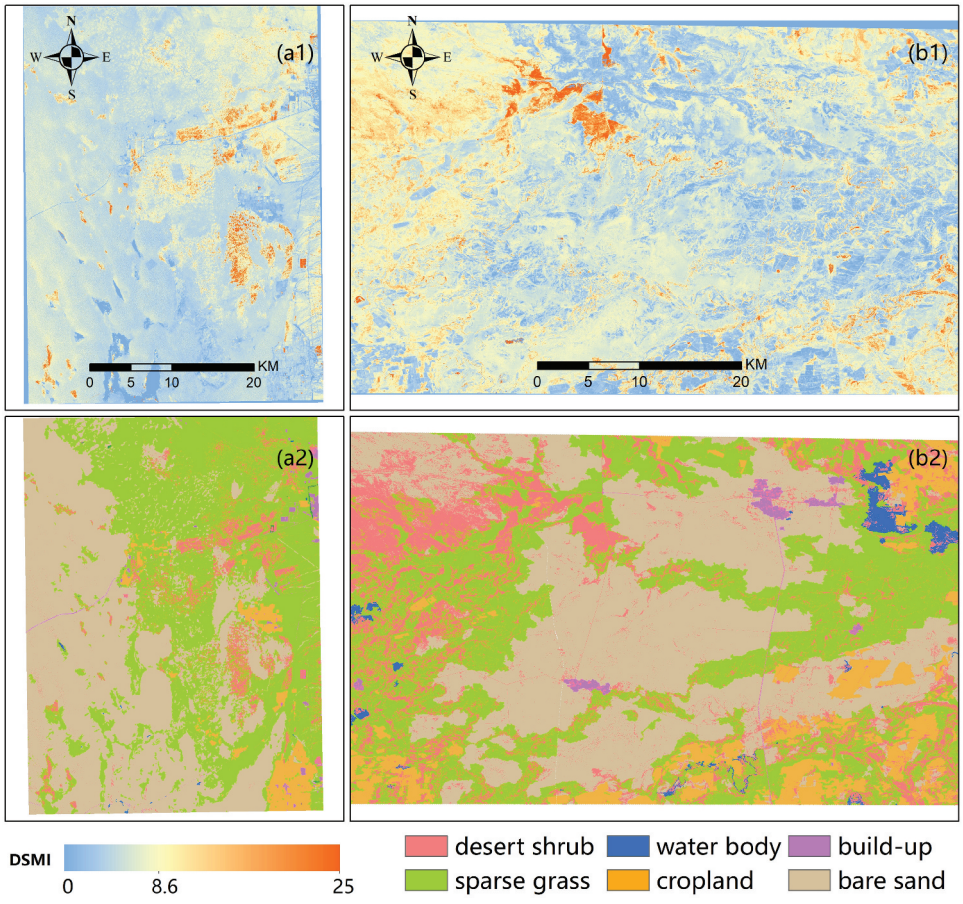


Figure 14. DSMI images of the test site in Alxa East County (a1) and Bugur County (b1), as well as the corresponding desert shrub results for these two regions (a2&b2). The desert shrubs are highlighted in red.

leaves of desert shrubs in Bugur County, which reduced the spectral influence from desert shrub branches and may also have led to a decrease in the DSMI value of local desert shrubs.

5.3. Advantages and limitations

The DSMI has the following advantages. It effectively supports systems for monitoring desertification via Earth observation satellite data. First, the proposed index is suitable for most medium-resolution imagery, which is the main data source for large-scale mapping of desert shrubs. Desertification is the result of long-term interactions between natural and socioeconomical activities, and approximately 25% of the world's drylands are threatened by desertification (D'Odorico et al. 2013; Lyu et al. 2020). In China, the economic loss caused by desertification is estimated at US$6.8 billion per year (Zhang 1996), all of which increases the need for desertification monitoring and management. Desert shrubs are the predominant vegetation type in arid desert regions and the primary vegetation type planted in afforestation projects in northwestern China (Wu et al. 2024). Desert shrubs play an important role in windbreaks and sand fixation, maintaining the stability of desert ecosystems and desertification management (Hu et al. 2021a; Hu et al. 2021b; Lan et al. 2021; Ward et al. 2018). In this study, we proposed a set of DSMI indices suitable for Landsat and Sentinel-2 images by analyzing the canopy spectra of desert shrubs and combining their growth phenology characteristics. The index can enhance the spectral signal of desert shrubs and quantify their coverage or probability in mixed pixels, facilitating the monitoring of desert shrubs in arid desert regions.

Second, the DSMI relies only on blue, near infrared/red edge and shortwave infrared bands, which are common bands in medium-resolution data. This indicates that the index can fully exploit vast amounts of historical remote sensing imagery (e.g. Landsat and Sentinel-2 imagery), demonstrating significant potential in the study of the historical dynamics of desert

shrubs. The successful extraction of desert shrubs via DSMI supports the view that accurate and rapid extraction of desert shrubs can be achieved by mining canopy spectra from optical data, without relying on structural information from SARs. The DSMI method provides a new paradigm for the historical dynamic study of desert shrubs and other land cover types.

Although the construction of indices with clear physical meaning is an effective method for desert shrub identification, it would also be beneficial to consider machine learning (ML) methods, which are now commonly used for land cover classification (Baumann et al. 2018; Gong et al. 2013; Rüetschi et al. 2021; X. Zhang et al. 2021). The ML method does not necessitate the construction of complex indices and enables the classification of land covers based on existing indicators. It can also identify the features that are more important during the classification process (Bartold et al. 2024a). Nevertheless, the relationship between ML and index construction is not a zero-sum game. Conversely, as Wang et al. (2022) reported, indices with clear physical meanings can provide more powerful features for ML methods. Similarly, our findings demonstrate that the classification performance can be further enhanced by replacing the most critical features with DSMI indices in the RF classifier. Furthermore, indices can be employed to provide intuitive explanations and aid in the validation of ML decision processes. Index construction is also a useful process for reducing the feature space and simplifying the ML models (Maxwell, Warner, and Fang 2018). Therefore, indices with clear physical meanings constitute an effective complement and aid in ML.

However, there are also several limitations. First, the index is susceptible to cloudy and rainy weather. Cloudy and rainy weather not only limits the acquisition of optical signals from desert shrubs but also notably impacts the feature values of the SWIR and NDMI. Fortunately, precipitation events in deserts tend to be sharp and temporary. During the long nongrowing season, interference from cloud cover and precipitation events can be easily avoided via image synthesis methods (Chu et al. 2021; Li et al. 2021). SAR data also offer a means to overcome this limitation, as they can provide crucial insights into shrub canopy structure and penetrate cloud and rain layers (Dąbrowska-Zielińska et al. 2012; Dabrowska-Zielinska et al. 2015). Consequently, future studies could consider integrating SAR data with traditional optical data to increase the continuity and reliability of desert shrub monitoring. Furthermore, although indices can visualize the spatial distribution of desert shrubs, it remains to be investigated how satellite-derived indices respond to climatically observed stresses, such as drought stress (Bartold et al. 2024b).

We also need to consider the impact of mixed pixels. The limitation of soil moisture limits the establishment and maintenance of continuous shrub cover (Mander et al. 2017; Smith et al. 2019; Tarnita et al. 2017). Thus, the desert shrubs identified in this study are actually a composite landscape of sand, grass and shrubs, with shrubs dominating the community (Figure 2b). The phenomenon of mixed pixels in these composite landscapes is inevitable. The mixed pixel effect could result in a disparate desert shrub coverage in pixels with the same index value. This implies that the threshold of 10.3 employed may result in the misclassification of pixels with low desert shrub coverage but high index values. This is precisely the source of omission and commission errors in the segmentation. In our study, we attempted to balance these two errors by reducing the difference between the UA and PA to reduce the impact of the mixed pixel effect on classification accuracy.

The generalization of the index to other arid regions is also important. Indeed, even for a given land cover type, there could be considerable spectral variation across different regions and different times. Such variations are particularly pronounced in natural land cover. Although the index can still effectively enhance the spectral differences between desert shrubs and background components, it is challenging to rely on a single threshold to achieve accurate segmentation of desert shrubs in different regions. Therefore, calibrating the threshold with field samples before applying the index to other regions is recommended, and the initial samples can be easily obtained by visual interpretation from high-resolution imagery, such as Google Earth images. Moreover, combining indices with ML methods may be a good practice. This could be achieved by labeling high-confidence desert shrub and non-desert shrub samples with the index image and then applying these samples to an ML algorithm for accurate segmentation.

6. Conclusions

Desert shrubs are the predominant vegetation type in arid desert regions and play essential roles in controlling wind erosion, carbon sequestration, and the stability of desert ecosystems. There is great practical value in large-scale spatial mapping of these shrubs. However, constrained by the spectral similarity between desert shrubs and sparse grasslands, as well as the mixed pixel effect inherent in medium-resolution remote sensing imagery, the mapping of desert shrubs at large scales remains a great challenge. In this study, we discovered sensitive features for desert shrub mapping, and then proposed a novel desert shrub mapping index based on the spectral and phenological characteristics of desert shrubs. The index was applied to desert shrub mapping in Ordos, a desert-steppe transition zone and effectively enhanced the spectral signal of desert shrubs on medium-resolution remote sensing data, achieving a satisfactory performance. To improve the applicability of the index, we also validated the applicability of this index to the Landsat-8 OLI sensor and in two test sites. This study not only lays the foundation for research on desert shrubs but also contributes to our understanding of desertification in arid regions and assists in assessing desertification risk.

Disclosure statement

The authors declare that they have no known commercial, personal and competing financial interest that have a conflict of interest with respect to this paper.

Funding

This research was supported by the National Natural Science Foundation of China (No. 41991232; No. 42071271) and the joint CAS-MPG research project (No. HZXM20225001MI).

ORCID

Zhijun Fu http://orcid.org/0009-0004-9662-8755

Data availability statement

The data that support the findings of this study are available on request from the corresponding author upon reasonable request.

References

Adams, J. B., M. O. Smith, and P. E. Johnson. 1986. "Spectral Mixture Modeling: A New Analysis of Rock and Soil Types at the Viking Lander 1 Site." *Journal of Geophysical Research: Solid Earth* 91 (B8): 8098–8112.

Ashourloo, D., H. S. Shahrabi, M. Azadbakht, H. Aghighi, H. Nematollahi, A. Alimohammadi, A. A. Matkan, et al. 2019. "Automatic Canola Mapping Using Time Series of Sentinel 2 Images". *ISPRS Journal of Photogrammetry and Remote Sensing* 156:63–76. https://doi.org/10.1016/j.isprsjprs.2019.08.007.

Ashourloo, D., H. S. Shahrabi, M. Azadbakht, A. M. Rad, H. Aghighi, and S. Radiom. 2020. "A Novel Method for Automatic Potato Mapping Using Time Series of Sentinel-2 Images." *Computers and Electronics in Agriculture* 175:105583. https://doi.org/10.1016/j.compag.2020.105583.

Bartold, M., and M. Kluczek. 2024a. "Estimating of Chlorophyll Fluorescence Parameter Fv/Fm for Plant Stress Detection at Peatlands under Ramsar Convention with Sentinel-2 Satellite Imagery." *Ecological Informatics* 81:102603. https://doi.org/10.1016/j.ecoinf.2024.102603.

Bartold, M., K. Wróblewski, M. Kluczek, K. Dąbrowska-Zielińska, and P. Goliński. 2024b. "Examining the Sensitivity of Satellite-Derived Vegetation Indices to Plant Drought Stress in Grasslands in Poland." *Plants* 13 (16): 2319.

Baumann, M., C. Levers, L. Macchi, H. Bluhm, B. Waske, N. I. Gasparri, and T. Kuemmerle. 2018. "Mapping Continuous Fields of Tree and Shrub Cover across the Gran Chaco Using Landsat 8 and Sentinel-1 Data." *Remote Sensing of Environment* 216:201–211. https://doi.org/10.1016/j.rse.2018.06.044.

Brandt, M., P. Hiernaux, T. Tagesson, A. Verger, K. Rasmussen, A. A. Diouf, C. Mbow, E. Mougin, and R. Fensholt. 2016. "Woody Plant Cover Estimation in Drylands from Earth Observation Based Seasonal Metrics." *Remote Sensing of Environment* 172:28–38. https://doi.org/10.1016/j.rse.2015.10.036.

Cao, H., L. Han, and L. Li. 2022. "Harmonizing Surface Reflectance between Landsat-7 ETM + , Landsat-8 OLI, and Sentinel-2 MSI over China." *Environmental Science and Pollution Research* 29 (47): 70882–70898.

Chang, J. G., M. Shoshany, and Y. Oh. 2018. "Polarimetric Radar Vegetation Index for Biomass Estimation in Desert Fringe Ecosystems." *IEEE Transactions on Geoscience and Remote Sensing* 56 (12): 7102–7108.

Chang, J., and M. Shoshany. 2017. "Radar Polarization and Ecological Pattern Properties across Mediterranean-To-Arid Transition Zone." *Remote Sensing of Environment* 200:368–377. https://doi.org/10.1016/j.rse.2017.08.032.

Chang, Q., S. Zwieback, B. DeVries, and A. Berg. 2022. "Application of L-Band Sar for Mapping Tundra Shrub Biomass, Leaf Area Index, and Rainfall Interception." *Remote Sensing of Environment* 268:112747.

Chen, H., H. Li, Z. Liu, C. Zhang, S. Zhang, and P. Atkinson. 2023a. "A Novel Greenness and Water Content Composite Index (GWCCI) for Soybean Mapping from Single Remotely

Sensed Multispectral Images." *Remote Sensing of Environment* 295:113679.

Chen, J., J. Chen, A. Liao, X. Cao, L. Chen, X. Chen, C. He, G. Han, S. Peng, M. Lu, and W. Zhang. 2015. "Global Land Cover Mapping at 30m Resolution: A Pok-Based Operational Approach." *ISPRS Journal of Photogrammetry and Remote Sensing* 103:7–27.

Chen, J., M. Yuan Zhang, L. Wang, H. Shimazaki, and M. Tamura. 2005. "A New Index for Mapping Lichen-Dominated Biological Soil Crusts in Desert Areas." *Remote Sensing of Environment* 96 (2): 165–175.

Chen, S., H. Ren, R. Liu, Y. Tao, Y. Zheng, and H. Liu. 2021. "Mapping Sandy Land Using the New Sand Differential Emissivity Index from Thermal Infrared Emissivity Data." *IEEE Transactions on Geoscience and Remote Sensing* 59 (7): 5464–5478.

Chen, Y.-N., K.-C. Fan, Y.-L. Chang, and T. Moriyama. 2023b. "Special Issue Review: Artificial Intelligence and Machine Learning Applications in Remote Sensing." *Remote Sensing* 15 (3): 569.

Chu, D., H. Shen, X. Guan, Chen, J., Li, X., Li, J., and Zhang, L., 2021. "Long Time-Series NDVI Reconstruction in Cloud-Prone Regions via Spatio-Temporal Tensor Completion." *Remote Sensing of Environment* 264:112632.

Dąbrowska-Zielińska, K., M. Budzyńska, W. Kowalik, I. Małek, M. Gatkowska, M. Bartold, and K. Turlej. 2012. "Biophysical Parameters Assessed from Microwave and Optical Data." *International Journal of Electronics and Telecommunications* 58 (2): 99–104.

Dabrowska-Zielinska, K., M. Budzynska, M. Tomaszewska, M. Bartold, and M. Gatkowska. 2015. "The Study of Multifrequency Microwave Satellite Images for Vegetation Biomass and Humidity of the Area under Ramsar Convention." In 2015 IEEE International Geoscience and Remote Sensing Symposium (IGARSS), Milan, Italy, (pp. 5198–5200)

Deng, C., and C. Wu. 2012. "BCI: A Biophysical Composition Index for Remote Sensing of Urban Environments." *Remote Sensing of Environment* 127:247–259.

D'Odorico, P., A. Bhattachan, K. F. Davis, S. Ravi, and C. W. Runyan. 2013. "Global Desertification: Drivers and Feedbacks." *Advances in Water Resources* 51:326–344.

Elvidge, C. D. 1990. "Visible and near Infrared Reflectance Characteristics of Dry Plant Materials." *Remote Sensing* 11 (10): 1775–1795.

Feng, X., R. Liu, C. Li, M. Li, Y. Wang, and Y. Li. 2022. "Multi-Level Physiological and Morphological Adjustment of Haloxylon Ammodendron Related to Groundwater Drawdown in a Desert Ecosystem." *Agricultural and Forest Meteorology* 324:109096.

Feng, X., R. Liu, C. Li, H. Zhang, and M. Slot. 2023. "Contrasting Responses of Two C4 Desert Shrubs to Drought but Consistent Decoupling of Photosynthesis and Stomatal Conductance at High Temperature." *Environmental and Experimental Botany* 209:105295.

Fensholt, R., and I. Sandholt. 2003. "Derivation of a Shortwave Infrared Water Stress Index from Modis near-And Shortwave Infrared Data in a Semiarid Environment." *Remote Sensing of Environment* 87 (1): 111–121.

Gibbens, R. P., and J. M. Lenz. 2001. "Root Systems of Some Chihuahuan Desert Plants."*Journal of Arid Environments* 49 (2): 221–63.

Gong, P., J. Wang, L. Yu, Y. Zhao, Y. Zhao, L. Lu, and Z. Niu. 2013. "Finer Resolution Observation and Monitoring of Global Land Cover: First Mapping Results with Landsat TM and ETM+ Data." *International Journal of Remote Sensing* 34 (7): 2607–2654.

Gorelick, N., M. Hancher, M. Dixon, S. Ilyushchenko, D. Thau, and R. Moore. 2017. "Google Earth Engine: Planetary-Scale Geospatial Analysis for Everyone." *Remote Sensing of Environment* 202:18–27.

Guo, X., and P. Li. 2020. "Mapping Plastic Materials in an Urban Area: Development of the Normalized Difference Plastic Index Using Worldview-3 Superspectral Data." *ISPRS Journal of Photogrammetry and Remote Sensing* 169:214–226.

Hellesen, T., and L. Matikainen. 2013. "An Object-Based Approach for Mapping Shrub and Tree Cover on Grassland Habitats by Use of Lidar and Cir Orthoimages." *Remote Sensing* 5 (2): 558–583.

Hu, X., X.-Y. Li, Y. Zhao, G. Zhou, and S. Zhao. 2021a. "Changes in Soil Microbial Community during Shrub Encroachment Process in the Inner Mongolia Grassland of Northern China." *Catena* 202:105230.

Hu, X., C. Song, X. Fan, Xiao Y., W. Xu, and Z. Ouyang. 2021b. "Main Regulation Services and Value Assessment of Shrub Ecosystem in China." *Journal of Beijing Foreign University* 20 (3): 58–64. https://doi.org/10.13931/j.cnki.bjfuss.2021073 .

Klemas, V., and R. Smart. 1983. "The Influence of Soil Salinity, Growth Form, and Leaf Moisture on-The Spectral Radiance of." *Photogrammetric Engineering and Remote Sensing* 49 (1): 77–83.

Knipling, E. B. 1970. "Physical and Physiological Basis for the Reflectance of Visible and near-Infrared Radiation from Vegetation." *Remote Sensing of Environment* 1 (3): 155–159.

Kopeć, D., and Ł. Sławik. 2020. "How to Effectively Use Long-Term Remotely Sensed Data to Analyze the Process of Tree and Shrub Encroachment into Open Protected Wetlands." *Applied Geography* 125:102345.

Laliberte, A. S., A. Rango, K. M. Havstad, J. F. Paris, R. F. Beck, R. McNeely, and A. L. Gonzalez. 2004. "Object-Oriented Image Analysis for Mapping Shrub Encroachment from 1937 to 2003 in Southern New Mexico." *Remote Sensing of Environment* 93 (1–2): 198–210.

Lan, S., A. D. Thomas, S. Tooth, L. Wu, and D. R. Elliott. 2021. "Effects of Vegetation on Bacterial Communities, Carbon and Nitrogen in Dryland Soil Surfaces: Implications for Shrub Encroachment in the Southwest Kalahari." *Science of the Total Environment* 764:142847.

Li, S., L. Xu, Y. Jing, H. Yin, X. Li, and X. Guan. 2021. "High-Quality Vegetation Index Product Generation: A Review of NDVI Time Series Reconstruction Techniques." *International Journal of Applied Earth Observation and Geoinformation* 105:102640.

Lundberg, S. M., and S.-I. Lee. 2017. "A Unified Approach to Interpreting Model Predictions." *Advances in Neural Information Processing Systems* 30.

Lyu, Y., P. Shi, G. Han, L. Liu, L. Guo, X. Hu, and G. Zhang. 2020. "Desertification Control Practices in China." *Sustainability* 12 (8): 3258.

Mander, L., S. C. Dekker, M. Li, W. Mio, S. W. Punyasena, and T. M. Lenton. 2017. "A Morphometric Analysis of Vegetation Patterns in Dryland Ecosystems." *Royal Society Open Science* 4 (2): 160443.

Mao, P., J. Ding, B. Jiang, L. Qin, and G. Qiu. 2022. "How Can Uav Bridge the Gap between Ground and Satellite Observations for Quantifying the Biomass of Desert Shrub Community?" *ISPRS Journal of Photogrammetry and Remote Sensing* 192:361–376.

Maxwell, A. E., T. A. Warner, and F. Fang. 2018. "Implementation of Machine-Learning Classification in Remote Sensing: An Applied Review." *International Journal of Remote Sensing* 39 (9): 2784–2817.

Middleton, N., and D. S. Thomas. 1997. *World Atlas of Desertification*. Arnold, London: John Wiley.

Rüetschi, M., D. Weber, T. L. Koch, L. T. Waser, D. Small, and C. Ginzler. 2021. "Countrywide Mapping of Shrub Forest Using Multi-Sensor Data and Bias Correction Techniques." *International Journal of Applied Earth Observation and Geoinformation* 105:102613.

Schulz, K., R. Hänsch, and U. Sörgel. 2018. "Machine Learning Methods for Remote Sensing Applications: An Overview." *Earth Resources and Environmental Remote Sensing/GIS Applications* IX (10790): 1079002.

Sen, R., S. Goswami, and B. Chakraborty. 2019. "Jeffries-Matusita Distance as a Tool for Feature Selection." In 2019 International Conference on Data Science and Engineering (ICDSE), Patna, India (pp. 15–20). IEEE

Smith, W. K., M. P. Dannenberg, D. Yan, S. Herrmann, M. L. Barnes, G. A. Barron-Gafford, and J. A. Biederman. 2019. "Remote Sensing of Dryland Ecosystem Structure and Function: Progress, Challenges, and Opportunities." *Remote Sensing of Environment* 233:111401.

Song P., Y. Zhang, J. Guo, J. Shi, T. Zhao, and B. Tong. 2022. A 1 km daily surface soil moisture dataset of enhanced coverage under all-weather conditions over China in 2003–2019. *Earth System Science Data* 14 (6): 2613–2637.https://doi.org/10.5194/essd-14-2613-2022

Tarnita, C. E., J. A. Bonachela, E. Sheffer, J. A. Guyton, T. C. Coverdale, R. A. Long, and R. M. Pringle. 2017. "A Theoretical Foundation for Multi-Scale Regular Vegetation Patterns." *Nature* 541 (7637): 398–401.

Teraminami, T., A. Nakashima, M. Ominami, M. Yamamoto, Z. Sheng, and K. Yoshikawa. 2013. "Effects of Sand Burial Depth on the Root System of Salix Cheilophila Seedlings in Mu Us Sandy Land, Inner Mongolia, China." *Landscape and Ecological Engineering* 9:249–257.

Tian, F., B. Wu, H. Zeng, X. Zhang, and J. Xu. 2019. "Efficient Identification of Corn Cultivation Area with Multitemporal Synthetic Aperture Radar and Optical Images in the Google Earth Engine Cloud Platform." *Remote Sensing* 11 (6): 629.

Tian, Y., B. Wu, W. Xu, J. Huang, and W. Xu. 2004. "An Effective Field Method of Crop Proportion Survey in China Based on Gvg Integrated System." In IGARSS 2004. 2004 IEEE International Geoscience and Remote Sensing Symposium, Anchorage, AK, USA (pp. 4028–4030). IEEE.

Wang, J., X. Cao, J. Chen, and X. Jia. 2015. "Assessment of Multiple Scattering in the Reflectance of Semiarid Shrublands." *IEEE Transactions on Geoscience and Remote Sensing* 53 (9): 4910–4921.

Wang, Z., B. Wu, M. Zhang, H. Zeng, L. Yang, F. Tian, Z. Ma, and H. Wu. 2022. "Indices Enhance Biological Soil Crust Mapping in Sandy and Desert Lands." *Remote Sensing of Environment* 278:113078.

Ward, D., J. Trinogga, K. Wiegand, J. Toit, D. Okubamichael, S. Reinsch, and S. Schleicher. 2018. "Large Shrubs Increase Soil Nutrients in a Semi-Arid Savanna." *Geoderma* 310:153–162.

Wu, B., Z. Fu, B. Fu, C. Yan, H. Zeng, and W. Zhao. 2024. "Dynamics of Land Cover Changes and Driving Forces in China's Drylands since the 1970S." *Land Use Policy* 140:107097.

Wu, B., J. Qian, Y. Zeng, L. Zhang, C. Yan, Z. Wang, A. Li, R. Ma, X. Yu, and J. Huang. 2017. *Land Cover Atlas of the People's Republic of China (1: 1 000 000)*. China Map Publishing House: Beijing. Chinese.

Xu, S., X. Zhu, J. Chen, X. Zhu, M. Duan, B. Qiu, and L. Wan. 2023. "A Robust Index to Extract Paddy Fields in Cloudy Regions from SAR Time Series." *Remote Sensing of Environment* 285:113374.

Xun, L., J. Zhang, D. Cao, S. Yang, and F. Yao. 2021. "A Novel Cotton Mapping Index Combining Sentinel-1 Sar and Sentinel-2 Multispectral Imagery." *ISPRS Journal of Photogrammetry and Remote Sensing* 181:148–166.

Yang, D., J. Chen, Y. Zhou, X. Chen, X. Chen, and X. Cao. 2017. "Mapping Plastic Greenhouse with Medium Spatial Resolution Satellite Data: Development of a New Spectral Index." *ISPRS Journal of Photogrammetry and Remote Sensing* 128:47–60.

Zhang, K., N. Guo, R. Wang, J. Si, and X. Wang. 2006. "Research on Spectral Reflectance Characteristics for Desert Meadow of Northwest China." *Advances in Earth Science* 21 (10): 1063.

Zhang, X., L. Liu, X. Chen, Y. Gao, S. Xie, and J. Mi. 2021. "GLC_FCS30: Global Land-Cover Product with Fine Classification System at 30 m Using Time-Series Landsat Imagery." *Earth System Science Data* 13 (6): 2753–2776.

Zhang, X., T. Zhao, H. Xu, W. Liu, J. Wang, X. Chen, and L. Liu. 2024. "GLC_FCS30D: The First Global 30 m Land-Cover Dynamics Monitoring Product with a Fine Classification System for the Period from 1985 to 2022 Generated Using Dense-Time-Series Landsat Imagery and the Continuous Change-Detection Method." *Earth System Science Data* 16 (3): 1353–1381.

Zhang, Y., D. Ning, and V. Smil. 1996. "An Estimate of Economic Loss for Desertification in China." *China Population Resource Environment* 6:45–49.

Zhu, Z., and C. E. Woodcock. 2014. "Continuous Change Detection and Classification of Land Cover Using All Available Landsat Data." *Remote Sensing of Environment* 144:152–171.